



VNIVERSITATIS VALÈNCIA

DOCTORAL PROGRAMME IN PHYSICS

Scaling symmetries and optimization of the
refractive index profile in optical fibers

AKTHAM TASHTUSH

Supervisors

PROF. ENRIQUE SILVESTRE MORA

PROF. MIGUEL V. ANDRÉS BOU

January 2019



VNIVERSITATIS VALÈNCIA

DOCTORAL PROGRAMME IN PHYSICS

Scaling symmetries and optimization of the
refractive index profile in optical fibers

Doctoral Thesis

AKTHAM TASHTUSH

Supervisors

PROF. ENRIQUE SILVESTRE MORA

PROF. MIGUEL V. ANDRÉS BOU

January 2019

Abstract

The optical fiber refractive index profile has a significant role in the optical devices fabrication like fiber Bragg gratings (FBG) and acousto-optic devices and the way guided light interacts in the presence of external factors like strain, stress or even bends. The analysis of the fiber profile gets to be feasible throughout understanding the properties of the optical guided modes such as the effective index, group index, and the chromatic dispersion. Taking a broader look at previous publications that use standard commercial optical fibers, it becomes noticeable that the ideal core-cladding step index profile gives incompatible results when it comes to the experimental versus the simulated dispersion curves. This difference is usually caused by various factors that changes the nominal geometrical and material parameters of the fiber. The stress resulted during the fabrication process, due to thermal and drawing effects is an example of many effects that causes the alteration of these parameters. In general, any irregularity in the fiber, geometrically speaking or material-wise, will produce a coupling of the energy of one mode to the others. Hence, studying coupled modes, whether they are induced by an inscribed FBG or an acousto-optic wave, provides useful information to test the effective refractive index profile required for an accurate theoretical simulation of fiber modes.

This research analyzes the characterization of the fibers refractive index profile and the effect of scaling transformation on the dispersion curves. A fiber scaling through two degrees of freedom, geometrical scaling and refractive index difference scaling, gives a significant improvement on fitting the simulated dispersion curves with the experimental ones. However, in many cases, an additional cladding alteration is also needed and shows effectiveness, especially when we analyze a wide wavelength range. According to our final results, a scaling in the geometrical properties of the core and a perturbation of linearly decreasing refractive index in the cladding

both describe the fiber profile correctly. As a consequence of our modified step index model, a perfect matching between the experimental and the theoretical dispersion curves is achieved. This process of fiber profile optimization, through the fiber scaling and cladding alteration, have also proven to be efficient, comprehensive and applicable for a wide range of commercial standard fibers.

Keywords: Optical fiber, dispersion curves, refractive index profile, scaling transformation, mode coupling, Bragg grating, acousto-optic interaction.

“And, when you want something, all the universe conspires in helping you to achieve it.”

— Paulo Coelho, *The Alchemist*.

Acknowledgments

First of all, I would like to offer my deepest appreciation to the group of fiber optics in the University of Valencia, on the whole. I will be always thankful for giving me the opportunity to be part of their research group and for investing in my potentials and supporting me all along the way. Hopefully this is not the end of the line but a start of further collaboration.

I convey my gratefulness to Prof. Enrique Silvestre, my supervisor and mentor in the last few years, whenever I needed anything academically or personally, his door was always open. He is unquestionably the finest supervisor I have ever had and undeniably one of the most perspicuous lecturers. In his patience, I had the courage to ask more and seek proficiency as he introduced me to the best methods of scientific research. In his vast comprehension of sciences, I encountered an endless fountain of knowledge and experience that made me a scientist way better than I was three years ago. I also express my sincere boundless gratitude to Prof. Miguel Andrés who was there for my help and guidance since day one, and was literally the first person to meet after stamping my first steps out of the plane when I arrived to Valencia.

I also owe many thanks to the members of my group, those who I worked with, relied on their experimental data or gave me advices in any way possible, for showing a fair sense of teamwork.

A special immeasurable thanks to the members of the 3D imaging group in the Department of Optics and to a couple of dear friends I had in the Institute of Material Sciences. Whether I cooperated with or did not, they all have granted me a friendly welcoming environment in and out of the University and they have never missed a chance of always helping me out and consistently making me feel included.

Always and forever, love and appreciation to my parents who have never stopped supporting me and have always been there for me through this long journey no matter what. Being away for those many years has been harder on them than it has on me, but with their limitless belief in me and the non-stopping encouragement, it has finally paid off.

To my brothers and sisters back home. We barely see each other but as their eldest brother, they have always put me on the spot, deemed as their role model, and that have given me anxiety in times, nonetheless, the determination and persistence to achieve more and do what makes me a better person for them to look up to.

Finally, and as far as boasting goes, to myself for the hard work along these last few years. I only hope that the experience I had through research and higher education would make me more self-aware and constructively critical of myself. Lawrence Bossidy once said, “Self-awareness gives you the capacity to learn from your mistakes as well as your successes. It enables you to keep growing”. Consistently my hopes are, by completing a new challenge in my life, to become more mentally grown and gain ownership of reality.

Un gran agradecimiento final a la Delegada de la Rectora para Estudiantes por su ayuda y apoyo en estos últimos meses, y a la Generalitat Valenciana y el comité de la beca Santiago Grisolia por su constante apoyo a los investigadores internacionales y la investigación científica.

“No creas todo lo que vean tus ojos. . . La imagen de la realidad que nos brindan nuestros ojos es sólo una ilusión, un efecto óptico”.

— Carlos Ruiz Zafón, *Las luces de septiembre*.

Resumen en español

Las fibras ópticas han revolucionado exitosamente el campo de las telecomunicaciones. Gran parte de ese éxito radica en las propiedades casi ideales que presentan las fibras ópticas, como son las bajas pérdidas por transmisión, el alto umbral de daño óptico y la baja no linealidad óptica (Agrawal, 2002; Kashyap, 1999). Estas propiedades han hecho realidad las comunicaciones rápidas a largas distancias.

La primera sección del Capítulo 2 de la tesis comienza describiendo el marco teórico en el que se va a trabajar: la ecuación de ondas, la teoría modal y la importancia de la descripción geométrica y la distribución del material en las fibras ópticas. Estos dos últimos conceptos, la geometría y los materiales empleados, nos permiten calcular cómo se comportan e interactúan los modos, ya estén guiados en el núcleo de la fibra o fuera de él.

En la segunda sección del capítulo, se resume el método iterativo de Fourier. Este método, que ha sido propuesto por el grupo de fibras ópticas de la Universidad de Valencia (LFO), es la base de nuestra herramienta de simulación numérica, y permite tratar con sistemas guidores que tienen una distribución de material compleja. Encontrar una solución al problema de guiado —un modo— en este método pasa por resolver las ecuaciones de valores propios que determinan las componentes transversales del campo eléctrico, \mathbf{e}_t , o del campo magnético, \mathbf{h}_t . Para ello, se utiliza el método de Arnoldi o el de Jacobi y Davidson, dado que ambos no requieren la representación explícita del operador asociado; es decir, es suficiente con poder evaluar la acción del operador sobre un vector arbitrario. El uso de la transformada rápida de Fourier (FFT) ayuda a pasar, de manera eficiente, entre el espacio de posiciones y el de frecuencias espaciales (o vectores de onda) en la evaluación de la acción del operador, espacios en los que las

diferentes partes de los operadores son diagonales. El método iterativo de Fourier es una opción perfecta cuando se trata de reducir la memoria y el tiempo de cómputo requeridos, además de permitir usar una solución anterior como semilla inicial para encontrar otras soluciones cercanas de manera eficiente.

A continuación, en la Sección 2.3, presentamos un nuevo desarrollo incorporado a nuestra herramienta de simulación que está basado en la presencia de simetrías *especulares* (con respecto a determinados planos) en la distribución material estudiada; asociada a esa simetría, la distribución del campo vectorial —p. ej., el campo eléctrico— puede mostrar un comportamiento *especular* o *antiespecular* respecto al mismo plano. Este proceso ayuda a reducir significativamente el tiempo de cálculo cuando se necesita una gran cantidad de modos de un tipo específico, como así fue en el trabajo recogido, más adelante, en el Capítulo 5. Teniendo en cuenta que los métodos de diagonalización mencionados calculan todos los vectores propios en un cierto rango de valores propios —lo que puede llevar mucho tiempo—, la consideración de las simetrías especulares en la distribuciones de campo permite, por un lado, reducir la dimensión de los vectores manejados entre un 50 % y un 75 %, y, por otro, limitar desde el principio el espacio de búsqueda de soluciones, reduciendo el número de modos que es necesario calcular en una proporción similar, lo que conlleva una reducción significativa en el tiempo de cálculo.

La última parte del capítulo resume la teoría de modos acoplados. Esta teoría intenta preservar el concepto de modo en situaciones en las que cualquier irregularidad en la fibra puede producir un acoplamiento de energía entre diferentes modos, lo que hace que la identificación del modo en un cierto ancho de banda sea un poco difícil. Cuando se satisface la condición de ajuste de fases, el acoplamiento entre modos propagantes se convierte en el concepto fundamental que usamos para describir las curvas de dispersión de los dos modos acoplados y de sus índices efectivos alrededor de las longitudes de onda de resonancia. Más adelante, las curvas de dispersión resultantes nos llevarán a una mejor comprensión de las propiedades de la fibra óptica a través de su perfil de índice de refracción.

El estudio del efecto que tiene en las propiedades de las fibras ópticas las modificaciones de sus distribuciones geométricas y materiales, permite determinar las mejores formas de fabricar, y eventualmente diseñar, los dispositivos ópticos y la manera en que la luz guiada interactúa con los diferentes materiales. Un procedimiento bien conocido para actuar sobre la luz en una fibra óptica consiste en inducir una perturbación periódica en el índi-

ce de refracción a lo largo de un tramo específico de la fibra. En el caso de las redes de Bragg de fibra (FBG), la modulación se logra mediante la irradiación con luz ultravioleta de fibras fotosensibilizadas (Vengsarkar et al., 1996; Lee & Erdogan, 2000). Las características de la modulación del índice de refracción desempeñan un papel clave en las propiedades espectrales de dicho dispositivo, principalmente la amplitud y el periodo de modulación; estas características y parámetros se han de fijar antes de iniciar el proceso de fabricación.

Otra forma de producir una modulación periódica del índice de refracción es propagar una onda acústica o elástica a lo largo de la fibra, lo que produce un cambio periódico del índice de refracción efectivo en ella ligado al efecto acustoóptico (Chang, 1976). El trabajo experimental en el que se basa el Capítulo 4 utiliza el concepto de interacción acustoóptica. La ventaja de esta interacción es que los parámetros de la modulación, y por lo tanto las características espectrales del dispositivo, pueden modificarse dinámicamente cambiando las propiedades de la onda elástica, sin alterar el material o la geometría de la fibra de forma permanente. La forma más clásica de generar una onda elástica a lo largo de una fibra óptica consiste en el uso de transductores piezoeléctricos y bocinas metálicas, que se han utilizado para este fin desde 1978 (Zemon & Dakks, 1978; Bates et al., 1985).

En la Sección 2.4, se revisa cómo las perturbaciones creadas en la fibra, ya sea por la onda acustoóptica, las redes de Bragg inscritas, o por cualquier otra técnica, son capaces de producir acoplamiento entre los modos ópticos guiados por la fibra. En las fibras monomodo, el acoplamiento se produce básicamente entre el modo fundamental, guiado por el núcleo, y un modo de la envoltura (Birks et al., 1996). En el caso de fibras de pocos modos, el acoplamiento también puede producirse entre el modo fundamental y un modo de núcleo de orden superior (Blake et al., 1987; Östling & Engan, 1995), mientras que en las fibras birrefringentes, el acoplamiento puede aparecer entre modos con polarización diferente por medio de ondas acústicas de torsión (Engan, 1996; Lee et al., 2007; Berwick et al., 1991).

En una red de Bragg de fibra, la modificación periódica del índice de refracción del núcleo de la fibra permite acoplar los modos propagantes a modos contrapropagantes. Los modos no tienen por qué ser idénticos, lo que significa que la FBG también puede convertir el modo fundamental en un modo de orden superior contrapropagante (Erdogan, 1997b; Lee & Erdogan, 2001). La FBG también puede convertir modos de orden superior en otros diferentes (Sáez-Rodríguez et al., 2011).

En una fibra monomodo, solo el modo fundamental está guiado dentro

del núcleo y todos los modos de orden superior están guiados por la envoltura. Una FBG inscrita en dicha fibra produce un acoplamiento multirresonante del modo del núcleo con modos de la envoltura contrapropagantes (Erdogan, 1997a), así como el acoplamiento intermodal de modos de la envoltura (Sáez-Rodríguez et al., 2011). Estos acoplamientos pueden ayudar a identificar las posibles deformaciones o tensiones presentes en la fibra, lo que permite una descripción más precisa del perfil de índice de refracción de la fibra. Como resultado del acoplamiento entre modos, el espectro de transmisión del modo del núcleo muestra una serie de picos de atenuación más o menos abruptos, a modo de las púas de un peine, para longitudes de onda más cortas que las de la resonancia de Bragg principal, entre el modo fundamental y el mismo modo contrapropagante. Las FBG con resonancias de los modos de la envoltura intensas han encontrado múltiples aplicaciones en la detección de variadas magnitudes (Guo et al., 2008; Martínez et al., 2005; Guo et al., 2009). Un ejemplo importante son los sensores de índice de refracción, que aprovechan el hecho de que los modos de la envoltura de alto orden radial son sensibles a las deformaciones y la curvatura de la fibra, así como al índice del medio que la rodea (Zhang et al., 2015; Jing et al., 2014). Por otro lado, se necesitan modos de la envoltura de orden azimutal alto para la detección direccional de curvaturas y torsiones (Thomas et al., 2012). Esto último solo se puede lograr con FBG que tengan una sección transversal asimétrica, y generalmente se logra inclinando la FBG en el núcleo respecto al eje de la fibra (Lee & Erdogan, 2001).

En cuanto a la interacción acustoóptica, también tiene aplicaciones en sensores de fibra, ya que el acoplamiento depende de la diferencia entre los índices efectivos de los modos ópticos acoplados y las características de la onda acústica; por lo tanto, es sensible a cualquier cambio de estos parámetros. Debido a su efecto sobre las propiedades acústicas de las fibras ópticas, la tensión es un parámetro para cuya medición es muy interesante usar estos métodos. Los sensores de tensión basados en la interacción acustoóptica funcionan de manera similar a los sensores de red de fibra de periodo largo (LPFG) (Lin et al., 2001). Las LPFG acoplan modos copropagantes con constantes de propagación próximas; por lo tanto, el periodo de dichas redes puede exceder considerablemente la longitud de onda de la radiación que se propaga en la fibra (Erdogan, 1997a).

El uso de la interacción acustoóptica permite estudiar fibras en su estado original, elimina la necesidad de disponer de un montaje para la escritura de las LPFG y agrega versatilidad gracias a su ajustabilidad (Lee et al., 2009; Pei et al., 2014). Hay muchos otros tipos de sensores de fibra que no se basan

en el acoplamiento de modos. Los sensores basados en interferometría, que son adecuados para la medida de temperatura o índice de refracción (Jung et al., 2011; Zhao et al., 2016), son un ejemplo de estos tipos.

Para aplicaciones en áreas tales como sensores, láseres, filtros u otros dispositivos utilizados en telecomunicaciones, la posibilidad de fabricarlos en la propia fibra ofrece muchas ventajas interesantes con respecto a los basados en elementos discretos insertados posteriormente en la fibra (Zou et al., 2013; Davis, 1985). En los componentes de fibra del primer tipo —hechos *solo de fibra*—, no es necesario extraer la luz guiada por la fibra óptica para, por ejemplo, procesar la señal en el dominio eléctrico, lo que conlleva menores pérdidas (Alcusa-Sáez, 2017). Los componentes ópticos tienen muchas otras ventajas; p. ej., la capacidad de cambiar dinámicamente las propiedades espectrales, como en el caso de la interacción acustoóptica, por ejemplo, nos permite controlar externamente las especificaciones de dichos dispositivos en tiempo real (Luo et al., 2007).

Las propiedades de los modos ópticos guiados por las fibras, como son el índice efectivo, el índice de grupo o la dispersión de la velocidad de grupo, son críticas en muchas aplicaciones. En los sistemas de telecomunicaciones ópticas, por ejemplo, la dispersión de la velocidad de grupo desempeña un papel clave en la calidad de las comunicaciones a larga distancia, ya que controla el ensanchamiento de los pulsos luminosos al viajar largas distancias; por ello, tener un conocimiento preciso de la dispersión cromática nos ayuda a abordar este problema adecuadamente.

Otro punto crucial en muchas aplicaciones es la caracterización de la homogeneidad axial de la fibra, particularmente de aquellas en las que se debe satisfacer una condición de ajuste de fase. Se han publicado varios métodos para la caracterización axial de las fibras ópticas, como los basados en la medida de luz retrodispersada utilizando refractómetros ópticos que trabajan en el dominio temporal (Vita & Rossi, 1979; Nakajima et al., 1997), o en el desajuste de fases en la mezcla de cuatro ondas (Mollenauer et al., 1996).

Por otro lado, el diseño de componentes de fibra como las redes de Bragg de periodo largo (Blake et al., 1986), los dispositivos acústicos ópticos en fibra (Kim et al., 1997), o cualquier otro dispositivo de fibra que involucre la interacción entre los modos del núcleo y de la envoltura requiere un conocimiento preciso de sus perfiles de índice de refracción. Además, la optimización de la multiplexación por división del espacio (SDM) (Rahman et al., 2018) basada en fibras ópticas de pocos modos requiere un modelado

preciso del espaciado de los modos, las longitudes de onda de corte, la dispersión cromática y otros parámetros importantes, que también dependen de los perfiles de índice de refracción.

Todo lo anterior justifica que las curvas de dispersión cromática tengan una enorme importancia, pues pretender encontrar un mejor ajuste para estas curvas a los datos experimentales en algún experimento, es comprender mejor las alteraciones en el perfil del índice de refracción de la fibra y, consiguientemente, poder predecir con precisión su comportamiento en otras situaciones. En nuestro caso, esto requiere que, partiendo de una cierta configuración inicial, vayamos modificando iterativamente el perfil de índice teórico hasta hacer cuadrar las predicciones con el experimento. En esta línea de trabajo, nuestro grupo obtuvo expresiones analíticas aproximadas para determinar el efecto del escalado geométrico de la fibra sobre su comportamiento cromático (Pinheiro Ortega, 2008). En el Capítulo 3 revisamos las aproximaciones necesarias que permiten obtener las ecuaciones mencionadas relativas a las curvas de dispersión cromática y a las de sus derivadas. Estas expresiones aproximadas se basan, en última instancia, en las propiedades de simetría de las ecuaciones de Maxwell cuando un sistema solo involucra materiales no dispersivos (Joannopoulos et al., 2008). Estas propiedades de simetría se pueden extender hacia un marco de trabajo menos restrictivo si, incluyendo materiales dispersivos, el comportamiento dispersivo de todos los materiales involucrados es parecido (Pinheiro Ortega, 2008). Como se muestra en los siguientes capítulos, las aproximaciones basadas en cambios de escala allanan el camino para que podamos controlar de manera eficiente las curvas de dispersión y estimar los parámetros estructurales adecuados para que la fibra óptica presente un cierto comportamiento a través de un par de factores de escala. En concreto, y en lo que respecta al núcleo de la fibra, el que da cuenta de la escala del radio del núcleo y el de la diferencia del índice de refracción entre el núcleo y su envoltura.

La introducción del escalado de la diferencia del índice de refracción se hizo, de hecho, en dos pasos. Por eso, en el Capítulo 4 se presenta utilizando un razonamiento heurístico, mientras que, en el Capítulo 5, la expresión analítica aproximada anterior se ha ampliado para incluir el nuevo grado de libertad, que, con la escala geométrica, forma una expresión completa que incluye ambos factores de escala.

En esta tesis, investigamos los perfiles de índice de refracción del núcleo y de la envoltura de las fibras para hacer coincidir las mediciones expe-

rimentales con las simulaciones teóricas. Los datos experimentales, representados por los índices efectivos y las resonancias de acoplamiento de los modos, se han recopilado mediante dos técnicas: la primera se basó en los acoplamientos acustoópticos analizados por [Alcusa-Sáez et al. \(2016\)](#), y la segunda se basó en los acoplamientos producidos por una red de Bragg inscrita en el núcleo de la fibra mediante radiación ultravioleta y analizada por [Poveda-Wong et al. \(2017\)](#). Para caracterizar adecuadamente las fibras analizadas, en los últimos capítulos de esta tesis, proponemos un perfil poco convencional pero simple que proporciona una muy buena coincidencia entre experimentos y simulaciones. La última parte de la tesis presenta varias simulaciones de los posibles ajustes en el perfil de la fibra. Estos ajustes se realizan primero a través de una transformación de escala en la geometría del núcleo de la fibra y del índice de refracción, y luego se completan introduciendo una perturbación en el índice de refracción de la envoltura.

En el Capítulo 4, tratamos los acoplamientos de modos linealmente polarizados inducidos por una onda acústica en dos fibras comerciales, SMF-28e y SM2000 ([Alcusa-Sáez et al., 2016](#)). Tras un análisis inicial del comportamiento de la curva de diferencias de índices efectivos del primer modo de la envoltura y del modo fundamental, LP_{01} - LP_{11} , es fácil reparar en que los resultados simulados empleando un modelo de salto de índice convencional para la fibra no pueden coincidir con los experimentales, por lo que nos propusimos, en un primer paso, hacer coincidir solamente el punto más característico de las curvas experimentales y de las simuladas: su máximo relativo, tanto la ordenada como la abscisa. Para ello, utilizamos una de las fórmulas obtenidas por [Pinheiro Ortega \(2008\)](#) para el escalado de la geometría y planteamos una dependencia lineal entre la diferencia de índices modales y la diferencia de índices en la distribución material para estimar el factor de escala relativo a la diferencia de índices entre el núcleo y la envoltura. Asimismo, para dar cuenta de las mejoras que logramos en el proceso de ajuste, definimos una función de mérito basada en el valor cuadrático medio del desajuste de las diferencias de índice efectivo.

El mero ajuste de los máximos de las curvas conlleva, en los casos analizados, una coincidencia perfecta para las curvas de diferencias de índices modales, pero solo en la región por debajo de la longitud de onda de corte del segundo modo ($\lambda < \lambda_c$), lo que implica que se ha conseguido una buena caracterización del núcleo de la fibra, pero no así de la envoltura. Para resolver la discrepancia para longitudes de onda grandes, introdujimos una perturbación en el índice de refracción de la envoltura, que, físicamente,

está originada por la tensión diferencial inducida durante la fabricación de la fibra (Violakis et al., 2012) y que puede modelizarse por una disminución lineal en el índice de refracción a lo largo del radio de la envoltura.

Después de unas pocas iteraciones, el nuevo modelo da lugar a una muy buena adaptación entre las curvas experimental y simulada, mejorando en un factor 10 el mejor ajuste obtenido considerando un modelo de salto de índice estándar, y eso se observó, tanto para las curvas de diferencias de índices efectivos, como para las de diferencias de dispersión de la velocidad de grupo. Este perfil de índice de refracción de fibra no convencional también ha demostrado que no solo ayuda a ajustar las curvas de dispersión para el primer modo acoplado, sino también para los modos más altos de la misma simetría (LP_{1m}).

Finalmente, en el último capítulo tratamos los acoplamientos modales activados por una red de Bragg inscrita en el núcleo de una fibra comercial SM1500 mediante luz ultravioleta (Poveda-Wong et al., 2017). Estos acoplamientos se presentan experimentalmente a través de un conjunto de estrechas depresiones en el espectro de transmisión del modo fundamental de iluminación, cada una a su longitud de onda de resonancia. Estas resonancias son fácilmente identificables en la región más alejada de la resonancia del modo de iluminación, que es la más nítida, pero cuanto más nos acercamos a ella, las resonancias aparecen más próximas entre sí y casi indistinguibles. Por ello, mediante la reescritura de la condición de ajuste de fases, desarrollamos una función de mérito que nos ha permitido identificar los modos asociados a cada resonancia en concreto. Seguidamente incorporamos a esa función de mérito la fórmula de escalado para determinar qué transformaciones de la estructura guiadora hacen que las curvas de índice efectivo simuladas pasen por los puntos obtenidos a partir de las resonancias experimentales. De esta forma, la función de mérito nos da una indicación sobre cómo escalar correctamente los parámetros del núcleo de la fibra —el radio del núcleo y la diferencia del índice de refracción—, para alcanzar el ajuste adecuado. En este punto de la investigación, se necesitaba calcular un gran número de modos guiados de una misma familia, por lo que fue necesario introducir en nuestra herramienta de simulación el filtrado basado en la simetría especular descrito en el Capítulo 2.

Para estudiar el efecto que produce en el perfilado de la fibra la limitación en el rango frecuencial muestreado por una red de Bragg, el proceso se ha aplicado primero a una única red de Bragg y luego a dos redes de Bragg de periodos diferentes grabadas en la misma fibra. Este proceso ha

demostrado ser eficiente en ambos casos al disminuir de 20 a 60 veces el desajuste promedio de las resonancias con las curvas simuladas. Finalmente se introdujo el mismo tipo de perfil de índice para la envoltura propuesto en el Capítulo 4, mostrándose una mejora adicional del 8% en el proceso de fijación de puntos de índice efectivo.

En consecuencia, hemos podido comprobar que un perfil tradicional de salto de índice, con distribuciones de índices de refracción constantes a trozos, no puede describir las curvas de dispersión de las fibras comerciales en banda ancha, y que es necesario introducir una perturbación en el índice de la envoltura. El origen físico de este desajuste es la tensión inducida durante la fabricación debido a los diferentes coeficientes de expansión térmica del núcleo y de la envoltura y la tensión inducida por el estirado de la fibra. El objetivo de esta investigación ha sido optimizar el modelo de salto de índice de la fibra óptica y presentar, utilizando simetrías de escalado y la alteración del índice de refracción de la envoltura, una descripción más realista del índice de refracción de la fibra, que proporciona una muy buena correspondencia entre los resultados experimentales y los teóricos. Este modelo permitirá diseños más precisos de redes de difracción de periodo largo, dispositivos acustoópticos y otros dispositivos que dependen de la participación de los modos de la envoltura de las fibras.

Todo este proceso de modificación de la envoltura y de escalado del núcleo de la fibra muestra la capacidad de ser coherente y aplicable para una amplia gama de fibras estándar comerciales.

Contents

Abstract	iii
Acknowledgements	vii
Resumen en español	xi
List of Figures	xxv
1 Introduction	1
2 Fundamentals of fiber optics and mode coupling	9
2.1 Mode theory and guided modes	9
2.2 Fourier iterative method	18
2.2.1 Wave equation derivation	19
2.2.2 Fourier iterative modal method	22
2.3 Mode Symmetry	24
2.4 Coupled mode theory	28
2.4.1 Bragg Gratings	29
2.4.2 In-fiber acousto-optics	32
3 Fiber profile scaling and dispersion curves	35
4 Optical fiber profiling based on scaling symmetries and acousto-optic mode coupling	39
4.1 Dispersion curves analysis	40
4.2 Controlling the core refractive index profile	43
4.3 Controlling the cladding refractive index profile	48
4.4 Fitting high order dispersion curves	54

5	Optical fiber profiling based on scaling symmetries and inscribed Bragg gratings modes coupling	57
5.1	Fiber profile scaling and dispersion curves	58
5.2	Refractive index profile scaling for a BG	59
5.3	Effective index fitting for a BG resonances	64
6	Conclusions	73
	Bibliography	86

List of Figures

2.1	3D scheme of step index optical fiber.	10
2.2	The effective refractive index as a function of V	13
2.3	The propagation constant β normalized as a function of V	14
2.4	LP ₀₁ and the two LP ₁₁ modes composition from their exact mode.	15
2.5	Effective index as a function of wavelength for the first set of modes in an optical fiber.	17
2.6	Effective index as a function of wavelength when an anti-crossing occurs.	18
2.7	<i>Mirror</i> and <i>anti-mirror</i> symmetry on a scalar field and a vector	25
2.8	Fiber Bragg gratings and the change occurred on the core refractive index.	30
2.9	Co-propagating and counter-propagating mode coupling.	31
4.1	The modal distribution of the fundamental mode LP ₀₁ and the first five modes of the type LP _{1m}	40
4.2	Simulated effective index difference curves, Δn_{eff} , for different values of NA and cutoff wavelengths.	41
4.3	The effective index difference curve, $\Delta n_{\text{eff}} = n_{\text{eff}}(\text{LP}_{01}) - n_{\text{eff}}(\text{LP}_{11})$, measured experimentally (solid blue curve) and the simulated one (dashed red curve) from Alcusa-Sáez et al. (2016)	42
4.4	Simulated effective index difference when the fiber core is scaled vs the experimental.	46
4.5	The original refractive index profile of a SMF-28e fiber (solid blue curve), from Abrishamian et al. (2012).	47
4.6	Power law index parameters effect on the fiber core profile.	48

4.7	Fiber refractive index profile with a ring perturbation in the cladding.	49
4.8	The simulated effective index difference curve after adding a ring perturbation in the cladding.	50
4.9	The simulated dispersion difference curve after adding a ring perturbation in the cladding.	51
4.10	The refractive index profile introducing a linear decline in the cladding refractive index.	52
4.11	The simulated effective index difference and dispersion difference curves when a perturbation of linearly declined refractive index is intruded in the cladding of a SM28-e fiber.	52
4.12	The value of χ with respect to the refractive index perturbation δn	53
4.13	The simulated effective index difference and dispersion difference curves when a perturbation of linearly declined refractive index is intruded in the cladding of a SM2000 fiber.	54
4.14	The simulated effective index difference curves for the first five modes compared to the experimental ones for a SMF-28e fiber when cladding perturbation is intruded.	55
4.15	The simulated effective index difference curves for the first five modes compared to the experimental ones for a SM2000 fiber when cladding perturbation is intruded.	56
5.1	Transmission spectrum for a Bragg grating (Poveda-Wong et al., 2017).	60
5.2	Modes identifying using a resonances assumption process.	64
5.3	The estimated effective index at the experimental resonance wavelengths of the first 20 modes of the type HE_{1m} and the simulated effective index curves for a BG.	65
5.4	The estimated effective index at the experimental resonance wavelengths of the first 20 modes of the type HE_{1m} and the simulated effective index curves for a BG after scaling the core.	66
5.5	Transmission spectrum for the first and the second Bragg gratings.	67
5.6	The estimated effective index at the experimental resonance wavelengths of the first 20 modes of the type HE_{1m} and the simulated effective index curves for BG #1 before and after the core scaling.	67

5.7	The estimated effective index at the experimental resonance wavelengths of the first 20 modes of the type HE_{1m} and the simulated effective index curves for the BG #2 before and after the core scaling.	68
5.8	The estimated effective index at the experimental resonance wavelengths of the first 20 modes of the type HE_{1m} pinned on the simulated effective index curves for both BGs after the core averging and rescaling.	70
5.9	The merit function value χ vs the introduced cladding perturbation δn	70
5.10	The estimated effective index at the experimental resonance wavelengths of the first 20 modes of the type HE_{1m} pinned on the simulated effective index curves for both BGs after introducing a cladding perturbation.	71

Chapter 1

Introduction

Optical fibers have successfully revolutionized the field of telecommunications. Much of that success lies in the fibers near ideal properties like low transmission loss, high optical damage threshold and low optical nonlinearity (Agrawal, 2002; Kashyap, 1999). These properties have made fast long distance communications a reality. The first part of Chapter 2 of the thesis starts by describing the theoretical framework of wave equation, mode theory and the importance of the geometrical description and material distribution in optical fibers. These last two properties, geometrical and material distribution, allow us to calculate how the modes behave and interact whether they are guided in the core of the fiber or in the cladding.

In the second part of the chapter, the Fourier iterative method is summed up. This method, which has been proposed by the group of fiber optics in the University of Valencia (LFO), is the base of our numerical simulation tool, which allows dealing with optical systems that have complex material structure. Finding a solution (mode) based on this method relies on solving the eigenvalue equations that determine the transverse components of the electric field, \mathbf{e}_t , or the magnetic field, \mathbf{h}_t . Using Fast Fourier Transform helps, in an efficient way, passing between momentum and position spaces while solving the related eigenvalue equations. The Fourier iterative method is a perfect choice when it comes to reducing the required memory as well as the computing time, add to that the ability to use a previous solution as an initial seed to efficiently find other neighboring solutions.

Later in Section 2.3, we also show a development on our simulation tool by having a proper classification of the modes based on their vector

field distribution symmetries. This classification is based on the *mirror* symmetry with respect to a specific plane: a *mirror*-like symmetry or an *anti-mirror*-like symmetry, all based on the vector — e.g., the electric field — behavior over the plane of symmetry. This process helps reducing the computational time significantly when calculating a very large number of a specific type of guided modes.

The last part of the chapter addresses the coupled mode theory. This theory attempts to preserve the mode concept where any irregularity in the fiber can produce a coupling of energy of one mode to another, which makes identifying the mode over a specific bandwidth somewhat challenging. When the phase matching condition is satisfied, coupling between propagating modes becomes the fundamental concept we use to describe the dispersion curves of the two coupled modes and their effective indices around the wavelengths of resonance. Later, the resulted dispersion curves will lead us to a better understanding of the optical fiber properties through the refractive index profile.

Studying the properties of the optical fiber, geometrically and material-wise, helps having a better understanding of the best ways of fabricating the optical devices and the way guided light interacts. A well-known procedure for light interacting in an optical fiber consists in producing a periodic perturbation of the refractive index along a specific section of the fiber. In the case of fiber Bragg gratings (FBG), it is achieved by means of the irradiation of photosensitive fibers with a UV light (Vengsarkar et al., 1996; Lee & Erdogan, 2000). The characteristics of the refractive index modulation plays a key role in the spectral properties of such device, mainly the modulation amplitude and period. These characteristics and parameters are set from the start ahead of fabrication.

Another way of producing a periodic modulation of the refractive index is propagating an acoustic or elastic wave along the fiber, which produces a periodic refractive index change along the fiber and an acousto-optic interaction occurs (Chang, 1976). The experimental work on which Chapter 4 is based uses the concept of acousto-optic interaction. The advantage of this concept is that the parameters of the modulation, and therefore the spectral characteristics of the device, can be dynamically modified through changing the elastic wave properties. The most classic way to generate an elastic wave along an optical fiber involves the use of piezoelectric transducers and metallic horns, which have been used for this purpose since 1978 (Zemon & Dakks, 1978; Bates et al., 1985).

In Section 2.4, it will be shown that the created perturbations in the

fiber, whether by the acousto-optic wave, the inscribed Bragg gratings, or by any other technique, are capable of producing coupling between the optical modes guided by the fiber. In single mode fibers, the coupling is basically produced between the fundamental core mode and a cladding mode (Birks et al., 1996). In the case of few-mode fibers, the coupling can also be produced between the fundamental mode and a higher-order core mode (Blake et al., 1987; Östling & Engan, 1995). While in birefringent fibers, the coupling can occur between modes with different polarization, by means of torsional acoustic waves (Engan, 1996; Lee et al., 2007; Berwick et al., 1991).

In a fiber Bragg grating, the periodic modification of the refractive index of the fiber core converts propagating modes into counter-propagating ones. The modes do not have to be identical, which means the FBG can also convert the fundamental mode into a counter-propagating higher order mode (Erdogan, 1997b; Lee & Erdogan, 2001). The FBG can also convert different higher order modes (Sáez-Rodríguez et al., 2011).

In a single mode fiber, it is known that only the fundamental mode is guided within the core and all higher order modes are guided by the cladding. An FBG inscribed in such fiber causes multi-resonant coupling of the core mode into counter-propagating cladding modes (Erdogan, 1997a) as well as inter-modal coupling of cladding modes (Sáez-Rodríguez et al., 2011). These couplings can help identifying the possible deformation, stress or strain that occurs in the fiber, which leads to more accurate description of the fiber refractive index profile. As a result of the mode coupling, the transmission spectrum of the core mode exhibits a series of dips, comb like, on the short wavelength side of the Bragg resonance. FBGs with strong cladding mode resonances have found widespread applications in sensing (Guo et al., 2008; Martinez et al., 2005; Guo et al., 2009). An important example is refractive index sensors, which exploit the fact that cladding modes of high radial order are sensitive to the deformations and bends of the fiber as well as the surrounding environment of the fiber (Zhang et al., 2015; Jing et al., 2014). On the other hand, cladding modes of higher azimuthal order are needed for directional sensing of fiber bends and twists (Thomas et al., 2012). The latter can only be achieved with FBGs that have an asymmetric cross-section. This is usually achieved by tilting the FBG in the fiber core (Lee & Erdogan, 2001).

As for the acousto-optic interaction, it also has applications in fiber sensors, since the coupling depends on the difference between the effective indices of the coupled optical modes and the characteristics of the acoustic

wave; therefore, it is sensitive to any change of these parameters. Due to its effect on the acoustic properties of optical fibers, strain is a parameter whose measurement holds a case of interest using these methods. Strain sensors based on acousto-optic interaction perform in a similar way to Long-period fiber grating (LPFG) sensors (Lin et al., 2001). LPFGs couple co-propagating modes with close propagation constants; therefore, the period of such gratings can considerably exceed the wavelength of radiation propagating in the fiber (Erdogan, 1997a).

Using the acousto-optic interaction eliminates the need of a LPFG writing setup and adding versatility thanks to their tunable features (Lee et al., 2009; Pei et al., 2014). There are many other types of fiber sensors not based on mode coupling. Sensors based on interferometry, which are suited for the measure of temperature or refractive index (Jung et al., 2011; Zhao et al., 2016), are an example of these types. As a characterization technique, acousto-optics does not introduce a material or geometrical change and, therefore, enables the study of pristine fibers.

For applications in areas such as sensors, lasers, filters, or other telecommunication devices, the fabrication of all-fiber components offers many interesting advantages with respect to those devices fabricated in bulk (Zou et al., 2013; Davis, 1985). In all-fiber components, it is not necessary to extract the light guided by an optical fiber to process the signal, therefore lower losses are introduced (Alcusa-Sáez, 2017). Acousto-optic components have many other advantages, the ability of dynamically change the spectral properties, for instance, allows us to externally control the specifications of such devices in real-time (Luo et al., 2007).

The properties of the optical modes guided by the fibers, such as the effective index, the group index or the chromatic dispersion, are of special interest since they are critical in many applications. In optical telecommunication systems, for instance, the chromatic dispersion plays a key role in the quality of long distances communications. Chromatic dispersion controls the broadening of signal pulses after traveling long distances, which indicates that having a near exact knowledge of the chromatic dispersion helps us tackle this issue.

Other crucial point in many applications is the characterization of the fiber axial homogeneity, particularly those in which a phase-matching condition must be satisfied. Recently, several methods have been reported for the axial characterization of optical fibers, such as the measure of backscattered light through optical time domain reflectometry (Vita & Rossi, 1979; Nakajima et al., 1997) or the mismatch of four-wave mixing (Mollenauer

et al., 1996).

In Chapter 3 we review several approximations to describe how the geometrical change of the fiber structure will affect the dispersion curves and its derivatives. These approximated expressions are initially based on the symmetry properties of Maxwell's equations when a system only involves non-dispersive materials (Joannopoulos et al., 2008). Afterwards, these symmetry properties progress into a less restrictive framework when it includes dispersive materials if the dispersive behavior of these materials act in a non-dispersive way with respect to a reference material (Pineiro Ortega, 2008). The scaling approximations paves the way for us to efficiently control the dispersion curves and estimate the proper parameters for the optical fiber through a pair of scale factors, which perform a scaling transformation on the core radius and/or the refractive index difference.

Designing fibers components like LPFGs (Blake et al., 1986), in-fiber acousto-optic devices (Kim et al., 1997), or any fiber devices involving the interaction between core and cladding modes requires an accurate understanding of their refractive index profiles. Moreover, the optimization of space division multiplexing (SDM) (Rahman et al., 2018) based on few-mode optical fibers requires an accurate modeling of mode spacing, cutoff wavelengths, chromatic dispersion, and other important parameters, which also depend on the refractive index profiles.

In this thesis, we investigate the core and cladding refractive index profiles in order to match the experimental measurements with the theoretical simulations. Therefore, we present an unconventional yet simple profile that provides a very good match. The last part of the thesis presents various simulations of the possible adjustments in the fiber profile. These adjustments will be implemented through first a scaling transformation on the fiber geometry and refractive index, then by a particular perturbation in the cladding refractive index.

In Chapter 4, we deal with linearly polarized modes couplings induced by an acousto-optic wave. By analyzing the behavior of the effective index difference curves between the fundamental mode and some higher order modes, we manage to fit properly the experimentally determined dispersion curves with the simulated ones. First we define a proportional formula to help us find the scale factors for the fiber parameters, which in turn results a perfect match for the coupled modes index difference curve but only in the region below cutoff ($\lambda < \lambda_c$). Consequently, we move into introducing perturbations in the cladding after noticing that the effective index difference curve of the first cladding mode coupled with the fundamental

one, LP_{01} - LP_{11} , shows noticeable mismatch on the region above the cutoff wavelength.

To track the improvement we achieve in the fitting process, we define a merit function based on the root mean square of the effective index mismatch. Subsequently, we introduce a perturbation in the cladding, defined as of a declining refractive index. Physically, this perturbation is originated by the induced differential stress during the fiber fabrication (Violakis et al., 2012). This perturbation description has shown a good fitting of the dispersion curves with the experimental ones by 10 times better compared to the simulated fiber with an ideal step index model, and that was visually presented by both the effective index difference curve and the dispersion difference curve. Later on, we show that this perturbation not only helps fitting the dispersion curves for the first coupled mode, but also for the higher modes of the same symmetry (LP_{1m}). This whole fiber scaling and cladding modification process shows the ability to be comprehensive and applicable for a wide range of commercial standard fibers.

Finally, on the last chapter we deal with the mode couplings triggered by UV-photo inscribed Bragg gratings. These couplings are experimentally presented through a set of notches each at its resonance wavelength. These resonances are easily identifiable over the region furthest from the fundamental mode resonance but the closest we get to the fundamental mode, the modes resonances become intensely packed and indistinguishable. Therefore, using an extension of the phase matching condition, we develop a formula that helps us identify these resonances and then modify the formula to properly pin the estimated effective index points at these experimental resonances on the simulated effective index curves. The formula is basically a merit function that gives us an indication on how to properly scale the fiber parameters, core radius and refractive index difference, to reach the suitable fit. This process has been applied on a single Bragg grating and then on two gratings each with different period, and it has proven to be efficient on both cases. We finally went further into identifying the stress effect in the cladding. Based on the same proposed cladding profile presented in Chapter 4, we have introduced a perturbation that, eventually, have shown an additional 8% improvement in the estimated effective index points pinning process.

Consequently, we realized that the traditional simple step index fiber profile with constant refractive indices distribution would not be able to model the dispersion curves of the core and cladding modes in commercial fibers and in a broadband. The physical origin of this mismatch appears to

be the stress induced during fabrication due to different core and cladding thermal expansion coefficients and drawing induced stress (Violakis et al., 2012). The purpose of this research is to optimize the step index model of the optical fiber and present, using the scaling symmetries and cladding refractive index alteration, a more realistic refractive index profile, which provides a very good match between the experimental and theoretical results.

Chapter 2

Fundamentals of fiber optics and mode coupling

This chapter consists of four sections. The main goal in the first section is to present some of the fundamental concepts of optical fiber starting with the basic laws that govern transmission and guidance of light in the fiber. The second section is set out to explain the calculating method used in our computational tool to solve the guided modes in some of the complex optical structures. Later in the third section we present an improvement on that computational tool using a proper modes classification based on their field distribution. Finally, we introduce the coupled mode theory and the way it affects the modes properties.

2.1 Mode theory and guided modes

The optical fiber is known to be a form of dielectric waveguide that operates at optical frequencies. This fiber waveguide is normally cylindrical in form and it has a central core, in which the light is guided, embedded in an outer cladding of lower refractive index. Figure 2.1(a) shows a 3D scheme of the optical fiber and a cross section of the structure.

The fiber confines electromagnetic energy in its core in form of light and guides it parallel to its axis. The guidance properties of dielectric systems are well discussed in the literature, and a complete analysis of them can be found, in many references (see, e.g., [Gowar, 1993](#); [Keiser, 2000](#); [Snyder &](#)

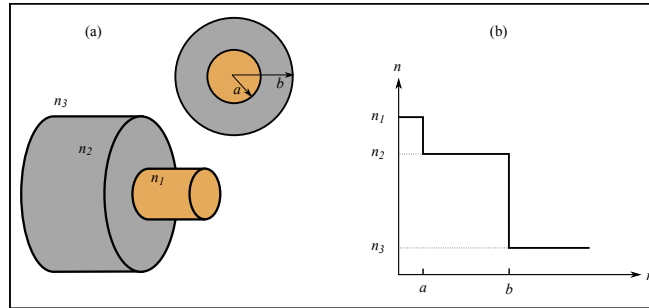


Figure 2.1: Figure (a) shows a 3D scheme of a step index optical fibers with its cross-section (up), while in (b) is the step index refractive index profile.

Love, 1983).

The structural characteristics of the optical fiber are very important and have a significant effect in knowing how the optical signal is affected while propagating in the fiber. Later in the next chapter, more details on the effect of the fiber structure on the behavior of guided modes will be presented.

In the case where the fiber is cylindrical with a standard step index profile, as shown in Figure 2.1(b), it has three different regions with constant refractive index: the core of the fiber, when $r < a$, with refractive index n_1 ; the cladding, when $a < r < b$, with refractive index n_2 , immersed in an external medium (usually air), when $r > b$, with refractive index n_3 , noting that $n_1 > n_2 > n_3$.

The optical mode is a particular pattern of electromagnetic field distribution of radiation measured in a plane perpendicular (i.e., transverse) to the propagation direction of the beam. Transverse modes occur because of boundary conditions imposed on the wave by the waveguide. The mode guided by the kind of fibers described previously can be calculated by solving the basic equations that governs the electromagnetic field dynamics in the fiber, that is, Maxwell's equations satisfying the corresponding boundary conditions. Taking into account that the systems, we are going to deal with, are in a medium without free charges or currents and no magnetic properties, $\rho = 0$, $\mathbf{J} = 0$ and $\mu = \mu_0$, these equations can be written as

$$\nabla \mathbf{H} = 0, \quad (2.1)$$

$$\nabla(\varepsilon\mathbf{E}) = 0, \quad (2.2)$$

$$\nabla \times \mathbf{E} = -\mu_0 \frac{\partial \mathbf{H}}{\partial t}, \quad (2.3)$$

$$\nabla \times \mathbf{H} = \varepsilon_0 \frac{\partial(\varepsilon\mathbf{E})}{\partial t}, \quad (2.4)$$

where \mathbf{E} and \mathbf{H} are, respectively, the electric and magnetic fields, ε represents the relative dielectric permittivity, ε_0 and μ_0 are respectively the vacuum permittivity and permeability.

On the other hand, when the medium does not change on time, as it is in our case, the fields \mathbf{E} and \mathbf{H} can be expressed as a linear superposition of harmonic fields on time. For each monochromatic component of frequency ω , Equations 2.3 and 2.4 become

$$\nabla \times \mathbf{E} = i\sqrt{\frac{\mu_0}{\varepsilon_0}}k_0\mathbf{H}, \quad (2.5)$$

$$\nabla \times \mathbf{H} = -i\sqrt{\frac{\varepsilon_0}{\mu_0}}k_0\varepsilon\mathbf{E}, \quad (2.6)$$

where $k_0 = \omega/c = 2\pi/\lambda$ is the wavenumber in vacuum and c is the speed of light in vacuum.

Additionally, in the case of guiding systems, in which the material distribution does not depend on, for instance, the z coordinate, fields can again be expressed as a linear combination of harmonic fields, but now on z , being the modes of the system those electromagnetic waves that propagate with defined frequency, ω , and propagation constant, β :

$$\mathbf{E}(\mathbf{x}, t) = \mathbf{e}(\mathbf{x}_t)e^{i(\beta z - \omega t)}, \quad (2.7)$$

$$\mathbf{H}(\mathbf{x}, t) = \mathbf{h}(\mathbf{x}_t)e^{i(\beta z - \omega t)}, \quad (2.8)$$

being

$$\mathbf{e}(\mathbf{x}_t) = \mathbf{e}_t + e_z \hat{\mathbf{u}}_z, \quad (2.9)$$

$$\mathbf{h}(\mathbf{x}_t) = \mathbf{h}_t + h_z \hat{\mathbf{u}}_z, \quad (2.10)$$

where $\hat{\mathbf{u}}_z$ is the unit vector in the z -axis direction, \mathbf{e}_t and \mathbf{h}_t are respectively the electric and magnetic components in the transverse direction, e_z and h_z are respectively the electric and magnetic components in the axial direction, and $\mathbf{x}_t = (x, y)$ are the transverse components of \mathbf{x} .

In general, depending on these previously mentioned components, the electromagnetic modes can be classified into different types. The modes where e_z component is equal to zero are called transverse electric modes, TE, and the modes where h_z component is absent are called the transverse magnetic modes, TM. Modes with zero e_z and h_z components are referred to as the transverse electromagnetic modes, TEM, and the modes with both e_z and h_z components different from zero are called hybrid modes, HE or EH.

A mode remains guided as long as its propagation constant β satisfies the condition

$$n_2 k_0 < \beta < n_1 k_0, \quad (2.11)$$

where n_1 and n_2 are the refractive indices of the core and the cladding respectively.

The light guidance through the optical fiber takes place due to the total internal reflection phenomenon, which allows the optical meridional ray to be transmitted in the core of the fiber through many reflections when it enters within a specific angle called the critical angle; this angle mainly depends on the material contrast between the core and the cladding:

$$\sin(\phi_c) = \frac{n_1}{n_2}. \quad (2.12)$$

A mode is referred to as being cutoff when it is no longer bounded to the core, so that its field no longer decays on the outside of the core. We can determine the number of modes that a fiber can support using an important parameter connected with the cutoff condition, the normalized frequency V , which is defined by

$$V = \left(\frac{2\pi}{\lambda} \right) a(\text{NA}), \quad (2.13)$$

where NA is the numerical aperture ($\text{NA} = \sqrt{n_1^2 - n_2^2}$) and a is the core radius.

Figure 2.2 shows a plot, from [Gloge \(1971\)](#), of the effective refractive index, $n_{\text{eff}} = \beta/k_0$ as a function of V for some of the low order modes. The plot, assuming a non-dispersive material, shows that each mode can exist only for values of V that exceed a certain limiting value. The modes are cutoff when the value of β/k_0 is equal to n_2 . The fundamental HE_{11} mode has no cutoff and ceases to exist only when V is zero ([Keiser, 2000](#)). Thereby, for any value of a , n_1 , and n_2 , there exists a certain wavelength,

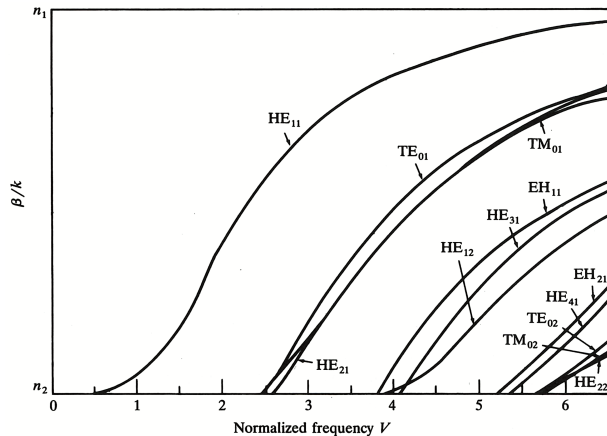


Figure 2.2: Plots of the effective refractive index, $n_{\text{eff}} = \beta/k_0$ as a function of V (Gloge, 1971).

λ_c , corresponding to a V value of 2.405, in which the fiber is considered a single mode fiber, i.e.,

$$V < \left(\frac{2\pi}{\lambda_c}\right)a(\text{NA}) = 2.405. \quad (2.14)$$

The exact analysis of the fiber modes is mathematically complex. However, a simpler yet highly accurate approximation can be used, using the fact that in a typical step index fiber the difference between the refractive indices of the core and the cladding is very small, that is, $n_1 - n_2 \ll 1$. This is the basis of the weakly guiding fiber approximation (Marcuse, 1991; Gloge, 1971; Snyder, 1969).

In this approximation, the electromagnetic field patterns and the propagation constants of the mode pair $\text{HE}_{v+1,m}$ and $\text{EH}_{v-1,m}$ are very similar (Keiser, 2000). This holds likewise for the three modes TE_{0m} , TM_{0m} , and HE_{2m} . This can be seen in Figure 2.2 as some modes are compacted in groups with $(v, m) = (0, 1)$ and $(2, 1)$ for the mode groupings (HE_{11}) , $(\text{TE}_{01}, \text{TM}_{01}, \text{HE}_{21})$, $(\text{HE}_{31}, \text{EH}_{11})$, (HE_{12}) , $(\text{HE}_{41}, \text{EH}_{21})$, and $(\text{TE}_{02}, \text{TM}_{02}, \text{HE}_{22})$.

A specific combination between these modes in the above-mentioned groupings would create a new type of modes. In Gloge (1971), it has been

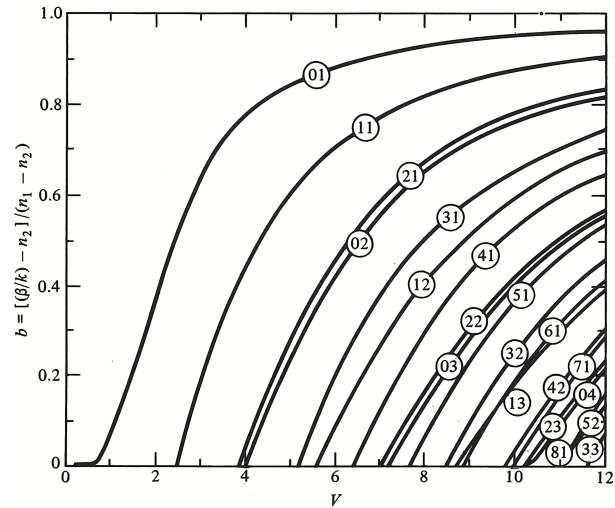


Figure 2.3: Plots of propagation constant β normalized as a function of V for various LP_{nm} modes (Gloge, 1971).

proposed that such degenerate modes be linearly combined to define quasi-linearly polarized fields and called linearly polarized (LP) modes, and be appointed LP_{nm} modes regardless of their TM, TE, EH, or HE field configuration.

When we work with standard optical fibers, like the one in Chapter 4, in which the mode degeneration is strong, it would be preferable to employ the linearly polarized LP modes. In this way, in the LP approximation, LP modes are linearly polarized modes, combination of quasi-degenerated TE, TM, EH and HE modes. The combinations are as follows:

- $HE_{1m} \Rightarrow LP_{0m}$,
- $(HE_{2m}; TE_{0m}; TM_{0m}) \Rightarrow LP_{1m}$,
- $(HE_{n+1,m}; EH_{n-1,m}) \Rightarrow LP_{nm} \quad (n \geq 2)$,

taking into account that each HE and EH modes are actually two orthogonally polarized degenerated modes. Similar to Figure 2.2, the propagation constant β normalized as a function of V for various LP_{nm} modes is shown in Figure 2.3 (Gloge, 1971).

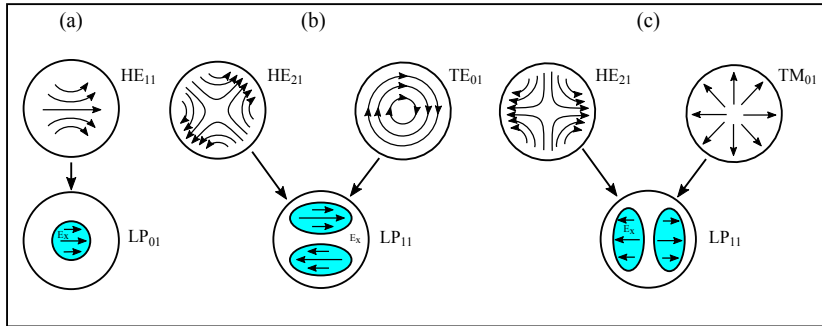
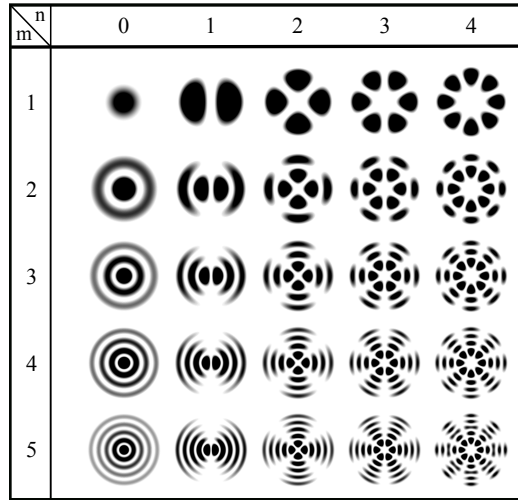


Figure 2.4: The LP₀₁ mode composition from its exact mode HE₁₁ polarized along x (a), and the two LP₁₁ modes compositions from exact modes and their transverse fields polarized along x (b and c).

A very useful feature of choosing the LP modes is the ability to easily visualize the mode. In a complete set of modes only one electric and another magnetic field component are significant. The electric field vector \mathbf{E} can be chosen to be along an arbitrary axis, with the magnetic field vector \mathbf{H} being perpendicular to it. In addition, when the field polarization is rotated it gives an equivalent solution. Figure 2.4 shows how the LP₁₁ modes are formed from the combination of the exact HE₂₁ and TE₀₁ modes, and the exact HE₂₁ and TM₀₁ modes, respectively, while the LP₀₁ mode is formed from the exact mode HE₁₁, where all of these LP modes are polarized along the x axis.

The Irradiance distribution of the first few LP _{nm} modes is shown in Table 2.1. As mentioned before, we should keep in mind that these modes represent one of the two possible polarizations. For instance, LP_{1 m} modes, each have a pair of modes polarized along the two coordinate axes perpendicular to the direction of propagation. Hence, the modal distribution in the figure are, as simulated, linearly polarized along the x axis, while the other LP twin mode with rotated polarization would have the same modal distribution rotated by 90° when polarized along the perpendicular y axis.

One of the most important properties the guided modes endure is dispersion. Even if non-dispersive materials are assumed, it is possible to make the speed of light dependent on wavelength by making light pass through a structure that has a non-constant refractive index profile, such as a waveguide. In this case, the waveform will spread over time, such that a narrow

Table 2.1: Irradiance distribution for various LP_{nm} modes.

pulse will become an extended pulse, i.e., be dispersed. This dispersion is related to the first derivative of the group velocity (Jenkins & White, 1957), which corresponds to the speed where the peak of the pulse propagates through space, which itself is related to a derivative of the phase velocity (Serway et al., 1957).

Based on Equation 2.14, optical fibers are usually characterized experimentally by two parameters: the numerical aperture, NA, and the cut-off wavelength of the first higher-order mode, λ_c , while in our analysis we use the core radius, a , and the difference of the squared refractive index, Δn^2 . Knowing these parameters, it is possible to calculate the dispersion relation of the different modes. In Figure 2.5, the dispersion relation has been calculated for a standard telecommunications fiber, an SMF-28e, with $\lambda_c = 1.4 \mu\text{m}$, NA = 0.12, a cladding diameter of $125 \mu\text{m}$, and taking into account the material dispersion (see end of Section 4.1) and assuming that the fiber is immersed in air ($n = 1$).

It is noticeable how the effective index of the fundamental mode lies between the effective refractive indices of the core and the cladding, n_1 and n_2 , while the other modes, the cladding modes, propagate with $n_{\text{eff}} < n_2$. The figure also shows the second mode when propagating with $n_{\text{eff}} > n_2$ for wavelengths below λ_c (the cutoff wavelength), being a core mode, while

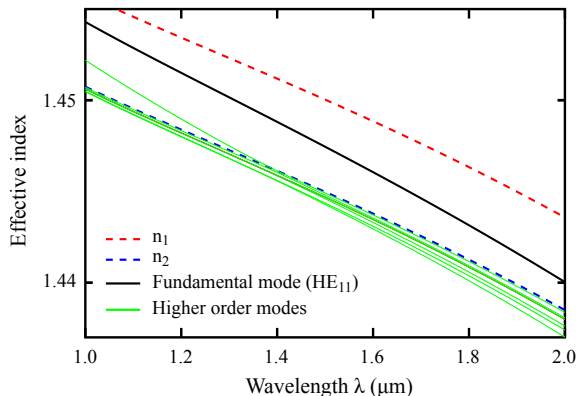


Figure 2.5: Effective index as a function of wavelength for the first set of modes in an optical fiber.

above λ_c it crosses the n_2 curve to propagate with $n_{\text{eff}} < n_2$, evolving to a cladding mode.

In the region where the mutual effect of the core and the cladding is strong, the modes trajectories can repel from one another. This means that calculating the dispersion relation might become tricky when two modes show similar effective indices at the same wavelength. These modes combines properties of the HE and EH modes.

Figure 2.6, a simulated case of the same SMF-28e fiber dealt experimentally by [Alcusa-Sáez \(2017\)](#), shows a close look on how the modes react when an anti-crossing is present. The second mode behaves as the HE_{22} for wavelengths below the anti-crossing wavelength, and as the EH_{21} above it, while the third mode behaves the other way around. At the region of the anti-crossing, the modes are no longer HE/EH but a mixed properties of both ([Light et al., 2008](#)). Section 2.4 summarizes this behavior through the mode coupling theory.

As shown previously through Figure 2.4, HE_{1m} modes are quasi-linearly polarized, from which the degenerate LP_{0m} modes are derived, and carry its intensity in the core. Increasing the radial order will decrease the modes quasi-linearly polarized character, which means that the polarization near the nodal rings becomes less linear. These LP_{0m} modes are the only case where the intensity is different from zero at the core center and its maximum lies at $r = 0$. A specific case is the fundamental mode, LP_{01} , always guided

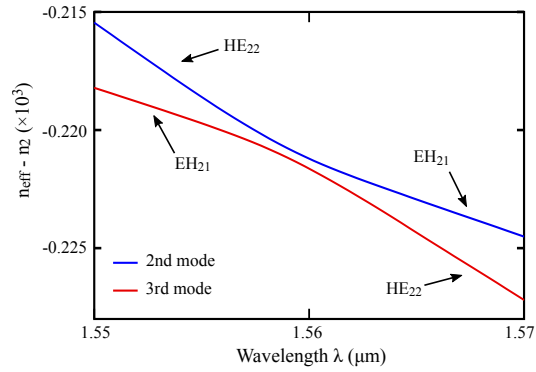


Figure 2.6: Effective index as a function of wavelength for the second and third guided modes around the anti-crossing wavelength.

by the core, and the intensity decays exponentially beyond $r = a$. As a result, we can represent this mode by a Gaussian-like intensity profile, which makes it different from the other modes. The fields of HE_{nm} modes are radial for angles π/n and azimuthal for the angle bisectors [see Figure 2.4] (Alcusa-Sáez, 2017).

The characteristics of the modes HE_{2m} , TE_{0m} and TM_{0m} are similar, and as previously explained, these three modes are part of the LP_{1m} modes formation. Similar to the TE and TM modes, HE_{2m} modes carry intensity in the fiber core, $r < a$. For both LP_{0m} and LP_{1m} modes, by going back to Table 2.1, it is noticeable that the ratio of Poynting vector flux (i.e., power flux) in the core with respect to the total carried power increases with the radial order of the mode (Paurisse et al., 2012). For all modes, it is important to keep in mind that the ratio of power flux in the core with respect to the cladding depends on the wavelength, especially around the cutoff wavelength of the fiber.

2.2 Fourier iterative method

Recently there have been a broad theoretical and experimental developments on optical systems with complex material structure, like in the case of photonic crystals or optical fibers with inhomogeneous refractive indices distribution. These developments have required numerical simulation tools.

These tools allow obtaining the electromagnetic fields and the key parameters that provide a general description of the system, which ultimately, give us the ability to design and optimize the structure.

If analytical solutions are available in sub-domains with compatible boundary conditions, the mode propagation constant can be obtained through the zeros of a relatively simple characteristic function, as it is the case of step index fiber (Snyder & Love, 1983). However, when the analytical solutions are not available whether due to nontrivial boundary conditions or due to inhomogeneous material distribution in the system, another type of methods is needed. The research group of Fiber Optics in the University of Valencia (LFO) has been working over the past years to develop a numerical tool implementing a Fourier iterative method. This tool, which is named *itera*, allows describing the propagation of the electromagnetic field in systems with translational symmetry and an arbitrary refractive index distribution in the transverse plane.

This section summarizes the theoretical foundations of the Fourier iterative method, by which all the analysis and simulations of this thesis project have been obtained.

2.2.1 Wave equation derivation

By going back to Equations 2.5 and 2.6 in the previous section, when we apply the curl operator and substitute one with the other, we obtain the wave equations for the electric and magnetic field, which are, respectively,

$$\nabla \times (\nabla \times \mathbf{E}) = k_0^2 \varepsilon \mathbf{E}, \quad (2.15)$$

$$\nabla \times (\varepsilon^{-1} \nabla \times \mathbf{H}) = k_0^2 \mathbf{H}. \quad (2.16)$$

Although \mathbf{E} and \mathbf{H} are tri-vectors, the fields governed by Equations 2.15 and 2.16 have only two degrees of freedom due to the constraints imposed by the Equations 2.1 and 2.2. For systems with translational invariance, i.e., $\varepsilon = \varepsilon(\mathbf{x}_t)$, it is simple to make this fact explicit, reducing the wave equations to systems of differential equations that only involve two components of the electromagnetic field (see Equations 2.7–2.10). The four remaining components are obtained from the previous ones by means of the constraints that establish the Maxwell equations between them, as it will be shown later in this section.

We are interested in the equations that satisfy the transverse components, either of the electric field, \mathbf{e}_t , or of the magnetic field, \mathbf{h}_t , since these could have the form of an eigenvalue equation. Finally, we choose to operate with \mathbf{h}_t since its components are continuous on the separation surfaces between dielectrics.

In the most common practical cases, the anisotropy of the materials that constitute our system is a block diagonal matrix and can be written as

$$\varepsilon = \begin{pmatrix} \varepsilon_{tt} & 0 \\ 0 & \varepsilon_{zz} \end{pmatrix}, \quad (2.17)$$

where ε_{tt} is the 2×2 submatrix corresponding to the transverse components of the dielectric tensor and ε_{zz} is a scalar associated to the longitudinal component. The dielectric tensor also takes this aspect in cases where an effective anisotropy is induced by the interfaces separating different isotropic media (Aspnes, 1982).

Taking these previous considerations into account, and combining Equations 2.7 and 2.8 while keeping Equations 2.9 and 2.10 in mind, we get the following expression for \mathbf{h}_t (Pinheiro Ortega, 2008),

$$\begin{aligned} \nabla_t \times [\varepsilon_{zz}^{-1}(\nabla_t \times \mathbf{h}_t)] - \hat{\mathbf{u}}_z \times [\varepsilon_{tt}^{-1}(\nabla_t \times \hat{\mathbf{u}}_z(\nabla_t \mathbf{h}_t))] \\ - \beta^2 \hat{\mathbf{u}}_z \times [\varepsilon_{tt}^{-1} \hat{\mathbf{u}}_z \times \mathbf{h}_t] = \frac{\omega^2}{c^2} \mathbf{h}_t, \end{aligned} \quad (2.18)$$

where ∇_t represents the transverse components of the gradient operator. The differential Equation 2.18 is an eigenvalue equation whose conventional resolution in the context of a modal approach passes through the representation of the operator associated with it in a certain basis for its subsequent diagonalization. However, this expression is not adequate to consider practical situations in which it is essential to take into account the material dispersion and/or the absorption loss, since the frequency itself is part of the eigenvalue to be determined. Therefore, after a series of mathematical algebraic simplifications made by Pinheiro Ortega (2008), we can finally reach the expression

$$\left[\nabla_t \nabla_t^T + \eta \varepsilon_{tt} \eta^T \left(\frac{\omega^2}{c^2} - \eta \nabla_t (\varepsilon_{zz}^{-1} \nabla_t^T \eta) \right) \right] \mathbf{h}_t = \beta^2 \mathbf{h}_t, \quad (2.19)$$

where the superscript T denotes the transpose of a matrix or a vector, depending on the element it accompanies, ε_{zz}^{-1} represents the longitudinal

component of the inverse of the dielectric tensor and η is the fully antisymmetric tensor in two dimensions,

$$\eta = \begin{pmatrix} 0 & 1 \\ -1 & 0 \end{pmatrix}. \quad (2.20)$$

In short, the Equation 2.19 is an eigenvalues equation so it can be rewritten symbolically as

$$L\mathbf{h}_t = \beta^2\mathbf{h}_t, \quad (2.21)$$

with

$$L \equiv \left[\nabla_t \nabla_t^T + \eta \varepsilon_{tt} \eta^T \left(\frac{\omega^2}{c^2} - \eta \nabla_t (\varepsilon_{zz}^{-1} \nabla_t^T \eta) \right) \right]. \quad (2.22)$$

In a similar way, the transverse components of the electric field can also be represented as

$$\left[\nabla_t \frac{1}{\varepsilon_{zz}} \nabla_t^T \varepsilon_{tt} + \left(\frac{\omega^2}{c^2} \varepsilon_{tt} - \eta \nabla_t (\nabla_t^T \eta) \right) \right] \mathbf{e}_t = \beta^2 \mathbf{e}_t. \quad (2.23)$$

If the field \mathbf{e}_t is rewritten in the form $\bar{\mathbf{e}}_t = (e_y^*, -e_x^*)$, the previous equation can be compacted as

$$L^\dagger \bar{\mathbf{e}}_{t(i)} = \beta^2 \bar{\mathbf{e}}_{t(i)}, \quad (2.24)$$

where L^\dagger is the adjoint operator of L (Silvestre et al., 1998). Although the evolution operator L is not generally self-adjoint, $L \neq L^\dagger$, even for non-absorbing media, this does not really represent a drawback for the implementation of a modal method since the eigenvectors of the nonself-adjoint operator, L , and the eigenvectors of its adjoint operator L^\dagger , fulfill the relationship of bi-orthogonality with the eigenvectors corresponding to the adjoint operator (Silvestre et al., 1998).

The property of bi-orthogonality allows performing a modal decomposition in waveguides whose refractive index profile is whether real or complex, including the study of waveguides with losses, and enabling the application to very different systems (Gantmacher, 1966; Morse & Feshbach, 1953). This fact is the key to continue operating in a conventional manner with projections and expected values. Bi-orthogonality have also been used successfully in bi-isotropic planar waveguide (Paiva & Barbosa, 1992) and laser resonators (Siegman, 1986). It is represented as

$$\langle \bar{\mathbf{e}}_{t(i)}, \mathbf{h}_{t(j)} \rangle = \delta_{ij}, \quad (2.25)$$

where $\langle \circ, \circ \rangle$ is the ordinary scalar product of complex vector functions in the plane xy , the subscripts i and j correspond to two different, non-degenerate modes. This property gives an understanding of the projections that the modal methods require (Silvestre et al., 1998).

After solving Equation 2.19 and obtaining the eigenvalues of the system, \mathbf{h}_t is known, the constraints that establish Maxwell's equations allow us to find, as previously pointed out, the rest of the components of the electromagnetic field. Thereby,

$$\mathbf{e}_t = \sqrt{\frac{\mu_0}{\varepsilon_0}} k_0^{-1} \varepsilon_{tt}^{-1} \mathbf{u}_z \times \left[\frac{1}{\beta} \nabla_t (\nabla_t \mathbf{h}_t) - \beta \mathbf{h}_t \right], \quad (2.26)$$

$$h_z = -i \sqrt{\frac{\varepsilon_0}{\mu_0}} k_0^{-1} (\nabla_t \times \mathbf{e}_t) \cdot \mathbf{u}_z, \quad (2.27)$$

$$e_z = i \sqrt{\frac{\mu_0}{\varepsilon_0}} k_0^{-1} \varepsilon_{zz}^{-1} (\nabla_t \times \mathbf{h}_t) \cdot \mathbf{u}_z. \quad (2.28)$$

With this set of equations, the necessary expressions are completed to obtain all the vector components of the electromagnetic field. For this reason, the modal representation method is completely vectorial, without approximations that could affect the precision of the calculations. The wave Equation 2.19 can also be extended to take into account the tensor nature of the magnetic permeability (Beltrán-Mejía, 2011). Introducing this property in the calculation tool, makes *itera* open to new possibilities also to work with materials and devices that contain anisotropic magnetic permeability like magnetic materials.

2.2.2 Fourier iterative modal method

As pointed out by the eigenvalue equation 2.24, for determining the electromagnetic fields of a fiber with an arbitrary material distribution, the operator L needs to be determined. For that purpose, and based on the work of Johnson & Joannopoulos (2001), the Fourier iterative modal method, developed by our group (LFO), takes advantage of different representation spaces to express the differential equation in form of a system of algebraic equations. More precisely, it uses the representation spaces where the different elements of the operator L are block diagonal matrices with 2×2 sub-matrices. Thus, the transverse gradient operator is block diagonal in the momentum space, while in the position space it is represented by a

dense matrix. On the contrary, the dielectric tensor, seen as an operator acting on the functions — the vectors — to which it multiplies, is block diagonal matrix with 2×2 sub-matrices in the position space and dense in the momentum space.

It is easy to pass between those two spaces using Fourier Transforms and the most efficient way to do it is through the so-called Fast Fourier Transform (FFT). The following diagram illustrates the use of FFT applied to the first term of the wave Equation 2.19,

$$\mathbf{h}_t \xrightarrow{[FFT]} \mathbf{k}_t \otimes \mathbf{k}_t^T \xrightarrow{[FFT^{-1}]} \nabla_t \nabla_t^T \mathbf{h}_t$$

These changes of the representation space are a critical step of the method due to the high number of occasions in which it has to be carried out. Fortunately, the Fastest Fourier Transform in the West algorithm (FFTW) (Frigo & Johnson, 1998) is not only very efficient, it also eliminates the traditional limitation of using powers of 2 in the number of sampling points. As a result of using Fast Fourier Transform, it is necessary to define a finite computational area that contains the relevant part the material distribution of the system. This area is in our case a square with side D , when replicated on the plane, creates a periodic and infinite transverse lattice. At the same time, the infinite replica of the cell creates a fictitious periodic medium in which the fields are described as Bloch waves (Joannopoulos et al., 2008).

In summary, it is important to note that the form of the operator L makes it possible to achieve that all its elements are diagonal in one or another representation space easily connected. This finding is key to solving the 2D wave equation without representing the operator explicitly, which leads to a huge reduction in memory requirements as well as computing time, allowing operation with fields sampled at hundreds of thousands of points in the cell.

The Fourier iterative method, summarized here, is also designed to deal with three-dimensional problems, although in our case the problem addressed is always two-dimensional, making it more efficient for the study of guiding systems. Using FFTs repeatedly, we can apply the L operator on the field without having to explicitly represent it as a matrix of dimensions $2N^2 \times 2N^2$. In this way, to carry out the calculation of the eigenvalue and eigenvector of L , and to solve the wave equation, Equation 2.19, we select an iterative numerical algorithm that requires only the vector resulting from the application of the related operator on the field.

This means, based on the method of Arnoldi and the construction of Krylov subspaces (Saad, 1992), we can also start from an initial field — the seed field —, which can give us after a series of iterations, a certain number of eigenvalues and eigenvectors of a certain range of the spectrum of the operator. We must re-emphasize that this type of algorithms are extremely efficient in terms of computational time.

On the other hand, the choice of seed field can greatly reduce the number of iterations and dramatically accelerate the convergence process. In many cases, the solution field of the scalar problem turns out to be very convenient as an initial field. That solution can be obtained by considering the weak guidance approach,

$$\left[\nabla_t^2 + \left(\frac{\omega}{c} \right)^2 n^2 \right] \mathbf{h}_t = \beta^2 \mathbf{h}_t, \quad (2.29)$$

and forcing linear polarization parallel to one of the coordinate axes. All this allows us to work with a large number of vectors of the base, and therefore, obtain extremely good results.

2.3 Mode Symmetry

Using the previously explained computational tool, the Fourier iterative method based, *itera*, is effective in finding almost all the possible guided modes in the optical waveguide. However, when aiming to analyze a high order of specific modes (like in our upcoming cases, LP_{1m} or HE_{1m}), the needed number of total modes to be calculated increases drastically, which consequently, means an increase in the computation time.

The other problem that rises is when we look for the higher order modes, finding a solution even with low precision becomes an issue, because as shown in Figure 2.5 the density of the modes increases as they become intensely compacted and their effective indices start to be very close to each other, and even after using the method explained at the end of the previous section (using an initial seed), we still face some difficulties and time consumption issues.

This calls for developing the computational tool in a way to reduce the number of calculated modes by filtering out the modes that are not of our interest. This change will make the density of the modes decrease and making it much easier for the computational tool to distinguish the required modes.

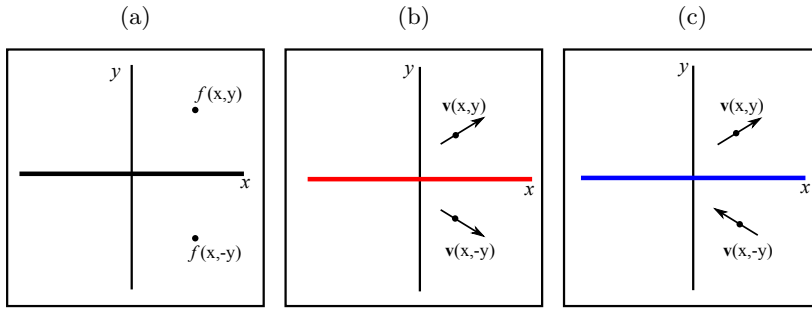


Figure 2.7: *Mirror* symmetry on a scalar field (a), the *mirror* symmetry on a vector $\mathbf{v}(x, y)$ (b), and the *anti-mirror* symmetry on a vector $\mathbf{v}(x, y)$ (c).

The way to do such thing is to introduce a filter of some sort where we can select the modes based on their field distribution. Starting from the characterization made by Schmidt & Petermann (2017:table II), which describes the modes of the graded index multi-mode fiber, we were able to reclassify a wide range of modes based on the symmetry properties of their vector field distributions: If a material distribution presents a *mirror* symmetry with respect to a given plane, the electric field distribution can present a *mirror*-like symmetry or an *anti-mirror*-like symmetry with respect to the same plane as it is illustrated in Figure 2.7.

When a mirror symmetry is satisfied by a scalar distribution, f , — as it is the case of the refractive index —, and considering the x axis as the mirror plane, then $f(x, y) = f(x, -y)$ for any point (x, y) [see Figure 2.7(a)]. The action of a mirror symmetry on a vector field, \mathbf{v} , — e.g., the electric field —, being again x the mirror plane, makes the field at (x, y) be related with the field at the reflected point by $\mathbf{v}(x, -y) = \mathbf{M}\mathbf{v}(x, y) = (v_x(x, y), -v_y(x, y))$ [Figure 2.7(b)]. On the contrary, the effect of an *anti-mirror* symmetry on a vector distribution [Figure 2.7(c)], forces the field at both sides of the mirror plane be linked through the expression $\mathbf{v}(x, -y) = \bar{\mathbf{M}}\mathbf{v}(x, y) = (-v_x(x, y), v_y(x, y))$.

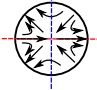
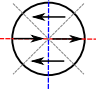
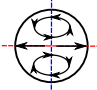
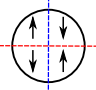

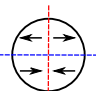
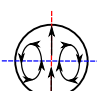
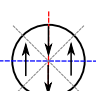

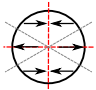
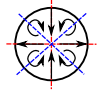
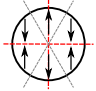

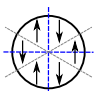

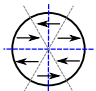
Table 2.2 shows two columns, categorized as a group of vector modes and LP modes that are derived of that group of vector modes. In the table, the red dashed lines represent a *mirror*-like axis while the blue dashed lines refers to the *anti-mirror*-like axis. As noticed, a mode might have multiple symmetry axes. In the particular case of systems with continuous rotational

symmetry, the increasing of the azimuthal order, l , is associated to the appearance of more symmetry planes. The gray dashed lines are placed in the zero field area that separates the modal intensity lobes, which gives a clue of how the modal distribution of the mode would look like.

Table 2.2: Symmetries of the vector field distribution for the first few modes.

		Vector Modes	LP Modes
$l=0, m=1$	HE _{1m} (even)		LP _{l,m} x (even)
	HE _{1m} (odd)		LP _{l,m} y (even)
$l=1, m=1$	HE _{2m} (even)		LP _{l,m} x (even)
	TM _{0m}		LP _{l,m} y (odd)
	HE _{2m} (odd)		LP _{l,m} x (odd)
	TE _{0m} (odd)		LP _{l,m} y (even)

Table 2.2 Continued

	Vector Modes	LP Modes
$l=2, m=1$	$HE_{l+1,m}$ (even) 	 $LP_{l,m} x$ (even)
	$EH_{l-1,m}$ (even) 	 $LP_{l,m} y$ (odd)
	$HE_{l+1,m}$ (odd) 	 $LP_{l,m} x$ (odd)
	$EH_{l-1,m}$ (odd) 	 $LP_{l,m} y$ (even)
$l=3, m=1$	$HE_{l+1,m}$ (even) 	 $LP_{l,m} x$ (even)
	$EH_{l-1,m}$ (even) 	 $LP_{l,m} y$ (odd)
	$HE_{l+1,m}$ (odd) 	 $LP_{l,m} y$ (even)
	$EH_{l-1,m}$ (odd) 	 $LP_{l,m} x$ (odd)

This process of identifying and categorizing the modes is then programmed into our computational tool. For the sake of simplicity, we have only considered mirror and anti-mirror reflections with respect to coordinate axes. In such way that, where we can choose a set of modes sharing a certain symmetry around one or two axes. As a result, this process helps us avoid calculating around 50% to in some cases 75% of unwanted modes, which will reduce the computational time significantly and helps easily reach large number of the desirable high order modes.

2.4 Coupled mode theory

Optical fibers support a finite number of guided modes and an infinite number of radiation modes. Coupling among the guided modes of a multimode optical waveguide (multimode waveguide refers to the guided modes) occurs when a perturbation is introduced and a mode of certain configuration changes the structure and converts into some other mode (Huang, 1994). Due to the induced perturbation in optical properties or geometrical configuration of the structure, a gratings for instance, or due to the imperfection of the materials used, we face the phenomena of mode coupling (Presby, 1977).

Coupling between guided modes and the continuum of radiation modes is usually not desired unless the waveguide is intended to serve as an antenna (Wang et al., 1995). However, a certain amount of coupling is unavoidable and results in scattering losses (Jones, 1965).

The coupled mode theory was first developed by Pierce (1954) and Miller (1954) in the early 1950's. It was until the early 1970's the coupled mode theory was introduced to guided-wave optics by Snyder (1972), Marcuse (1973), Yariv (1973), and Kogelnik (1975). The coupled mode theory has been very useful in understanding the nonlinear optical wave propagation and interaction, such as second harmonic generation, parametric amplification, and modulation instability (Shen, 1984; Agrawal, 1989). There are several reference textbooks available on the subject (see, e.g., Lee, 1986; Haus, 1984; Tamir, 1988; Shen, 1984; Agrawal, 1989).

The theory attempts to preserve the mode concept in situations in which the modes cannot be found (Snyder, 1972) due to the nonuniformity of the material along the propagation direction. In general, any irregularity in the fiber, such as, diameter variations, loss, and isolated particles, will produce a coupling of the energy or power of one mode to the others. Mode

coupling within an optical fiber causes signal contamination and is hence undesirable for optical communication systems. However, coupling can also occur between parallel fibers in fiber optics bundles (Kapany, 1967) and even between neighboring photoreceptors of mammalian and certain insect retinas (Lillywhite, 1978). Coupling can sometimes be used as an advantage by constructing optical devices such as the directional coupler (Louisell, 1960).

In this research, we use two methods to induce mode coupling, which help in studying the dispersion curves and eventually the fiber refractive index profile. The next two subsections will show how the dispersion relation curve represented by the effective refractive index is affected when two modes are coupled. In the first subsection we discuss the mode couplings induced by an inscribed fiber Bragg gratings while in Subsection 2.4.2 we review the mode couplings that are triggered by the acousto-optic interactions.

2.4.1 Bragg Gratings

Bragg gratings (BGs) are periodic perturbations in the fiber structure that couple energy between different modes. Figure 2.8 shows the change applied in the fiber which creates a perturbed core refractive index. They are classified in two categories: fiber Bragg gratings (FBGs), which operates at optical wavelengths at the material around twice the periodicity, Λ , (Hill et al., 1978), and long period fiber gratings (LPFGs), which are designed to work at wavelengths much shorter than the period (Blake et al., 1986).

The FBG couples energy at specific wavelengths between counter-propagating modes (core-core, core-cladding, cladding-cladding) (Sáez-Rodríguez et al., 2011; Erdogan & Sipe, 1996), while the LPFG couples energy between co-propagating modes (core-core, core-cladding) (Hill et al., 1990; Vengsarkar et al., 1996).

Gratings within fibers offer the possibility of chromatic and environmentally sensitive reflectivity which is of significance both to the sensor and optical communications communities (McCall, 2000). Bragg grating has become one of the most important fiber optic devices. Various applications that utilized Bragg gratings have been developed like mirrors, mode converters, filters, etc. In long period gratings, for instance, coupling into cladding modes has introduced additional degrees of freedom so that temperature, stress and strain deformations can be identified (Pang et al., 2008; Zangaro et al., 1995).

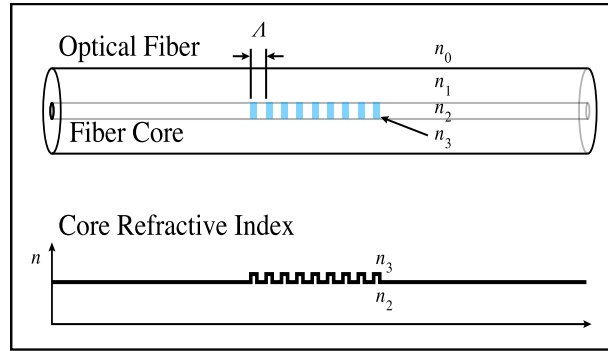


Figure 2.8: Fiber Bragg gratings and the change occurred on the core refractive index.

Fiber Bragg gratings have also been used for spectral filtering, wavelength tuning, dispersion compensation, and sensing in optical communication and optoelectronics (Vegsarkar et al., 1996; Liu et al., 2000). Just as gratings couple light from the guided fundamental mode to the counter-propagating core and cladding modes, it causes a set of loss notches in the transmission spectrum and, eventually, corresponding peaks in the reflection spectrum (Erdogan, 1999). The intensities of these peaks are determined by the UV induced index modulation of the core, the overlap between fundamental and cladding modes, and the length of FBGs.

The coupled mode theory is a widely used theoretical method to analyze fiber Bragg gratings (Erdogan, 1997b). By solving the coupled modes equation, we can obtain the transmission and reflection properties of fiber Bragg gratings with arbitrary grating structures. A simple model of a fiber Bragg grating is the following: The grating reflects a narrow band of the incident optical field by successive, coherent scattering from the index variations (Skaar & Waagaard, 2003). When the reflection from the crest in the index modulation is in phase with the next one, we have maximum mode coupling or reflection and the Bragg condition is fulfilled.

We can start with the equation of phase matching condition of two coupled modes in a grating mentioned by Kashyap (1999), i.e.,

$$\beta_{\mu}(\lambda_R) \pm \beta_{\nu}(\lambda_R) = \frac{2\pi N}{\Lambda}, \quad (2.30)$$

where $\beta_{\mu}(\lambda_R)$ and $\beta_{\nu}(\lambda_R)$ are the propagation constants of two coupled

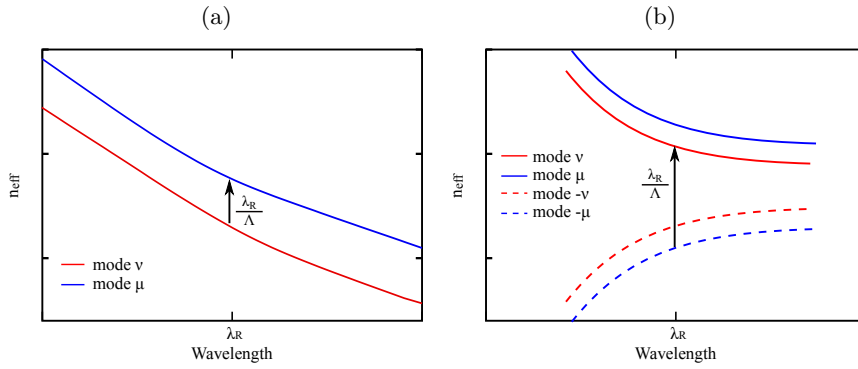


Figure 2.9: The coupling between mode ν and mode μ when (a) the modes are co-propagating and (b) the modes are counter-propagating.

modes, μ and ν , at the resonant wavelength λ_R , Λ is the period of the perturbation, and N is an integer ($-\infty < N < +\infty$) that signifies its harmonic order. Keeping in mind that $\beta(\lambda_R)$ could be written in terms of the effective index as $2\pi n_{\text{eff}}(\lambda_R)/\lambda_R$, and by only considering the first harmonic order, Equation 2.30 becomes

$$n_{\text{eff},\mu}(\lambda_R) \pm n_{\text{eff},\nu}(\lambda_R) = \frac{\lambda_R}{\Lambda}. \quad (2.31)$$

Figures 2.9 (a) and (b) show how the sign works in order to make sure that the phase matching condition is satisfied when two modes (μ and ν) are coupled. If the sign is negative then the phase-matching condition is satisfied for co-propagating modes, where $\Lambda[n_{\text{eff},\mu}(\lambda_R) - n_{\text{eff},\nu}(\lambda_R)] = \lambda_R$ as shown in Figure 2.9(a), meanwhile, as shown in Figure 2.9(b), if the sign is positive then the interaction is between counter-propagating modes, where

$$\Lambda[n_{\text{eff},\mu}(\lambda_R) + n_{\text{eff},\nu}(\lambda_R)] = \lambda_R. \quad (2.32)$$

This formula will be beneficial for us in Chapter 5 when we try to determine the real refractive index distribution of a given structure through its dispersion relation curves. Thus, we can conclude that the effective index of a mode μ when coupled with the illuminating mode at resonance wavelength $\lambda_{R,\mu}$ can be calculated by, simply, knowing the effective index of that illuminating mode at its resonance wavelength and the BG period.

2.4.2 In-fiber acousto-optics

The idea of acousto-optic interaction in an optical fiber resides in the coupling between fiber optical modes caused by an elastic wave when elastic waves were generated by a piezoelectric transducer (Zemon & Dakks, 1978). Experimentally, this piezoelectric transducer vibrates at the frequency of the electric signal, in a direction perpendicular to the axis of the fiber, which generates a flexural acoustic wave that propagates along the fiber with the frequency of the electric signal.

The fundamental flexural mode propagation in an optical fiber induces a periodic tension, whose periodicity corresponds to the spatial periodicity of the acoustic wave, Λ . This tension causes a perturbation in the refractive index through two contributions. First, there is a geometrical contribution, the stretching and compression physically vary the length of the fiber, and therefore the optical path of the guided light (Marcuse, 1982). On the other hand, there is the material contribution, as the tension modifies the refractive index of silica due to the elasto-optic effect (Smith, 1980). The effect combined of both contributions on the modal phase can be described considering that they create a change of an effective refractive index, n_{eff} (Block et al., 2006; Alcusa-Sáez, 2017).

Starting by the geometrical contribution, having $s = \Delta L/L$ as the relative stretching of the fiber in the axial direction where L is the length of the fiber, the effect of s in the effective index will be $\delta n_{\text{eff}} = n_{\text{eff}} s$. The change of the refractive index of the material caused by the elasto-optic effect, n , usually follows the form $\delta n = -ns\zeta$, where ζ the elasto-optic coefficient. Consequently, the contribution to the effective index change is represented as $\delta n_{\text{eff}} = -n_{\text{eff}} s\zeta$. By taking both contributions into account, the change in the effective index can be represented as (Alcusa-Sáez, 2017)

$$\frac{\delta n_{\text{eff}}}{n_{\text{eff}}} = (1 - \zeta)s. \quad (2.33)$$

Similar to the way the inscribed Bragg gratings works, these dynamic changes in the refractive index, when tuned properly, create coupling between the illuminating mode and the cladding ones resulting a notch for each coupling in the transmission spectrum. The notch can be adjusted by changing the wavelength of the acoustic wave, Λ , which can be done, experimentally, by simply changing the frequency of the RF signal transducer.

Very related to the purpose of this thesis, acousto-optic interaction has applications in the characterization of the properties of fibers themselves

(Díez et al., 2000; Haakestad & Engan, 2006). Ultimately, in Chapter 4 we use these mode couplings caused by the acousto-optic interactions to analyze the cladding refractive index profile.

Chapter 3

Fiber profile scaling and dispersion curves

Among the geometric transformation that can be applied to an electromagnetic system, (uniform) scaling is of special relevance as it relates systems that are similar (in the geometric sense), i.e., the distances between any pair of points of the original system are proportional, by a constant number, s — the scale factor —, to the corresponding distances of the transformed system. When the scale factor is larger than 1, the transformation *enlarges* the system; on the contrary, when s is a positive number smaller than 1, it *shrinks* it.

It is well known in electromagnetic theory that, assuming non-dispersive media, two systems related by a scaling transformation present solutions that are also related by the same transformation (Joannopoulos et al., 2008). The underlying scaling symmetry is broken when dispersive materials are involved. However, the symmetry can be partially recovered in guiding systems under certain conditions. This fact opens the possibility to adjust the optical properties of the system (Pineiro Ortega, 2008), and has been essential in the design of systems as complex as photonic crystal fibers (Silvestre et al., 2006; Ferrando et al., 2001).

In this chapter, we review a series of approximated analytical expressions that describe the propagation constant and its derivatives with respect to frequency in terms of the corresponding ones of the unscaled system and the scale factor (Pineiro Ortega, 2008). Some of these expressions will be of special interest and a practical starting point for the analysis and design

of the optical fiber and optical components, as it will be presented in the following chapters.

In order to reproduce the above mentioned approximated expressions, we can start with the 2D wave equation in the weak guidance approximation (Equation 2.29),

$$\left[\nabla_t^2 + \left(\frac{\omega}{c} \right)^2 n^2(\mathbf{x}_t, \omega) \right] \mathbf{h}_t = \beta^2 \mathbf{h}_t. \quad (3.1)$$

For simplicity, it has been considered that the dielectric tensor can be represented by a scalar function, $\varepsilon(\mathbf{x}_t, \omega) = n^2(\mathbf{x}_t, \omega)$, where $n(\mathbf{x}_t, \omega)$ represents the transverse spatial distribution of the refractive index of the unscaled system. Additionally, let us assume that we know the field distribution of a propagating mode and the corresponding propagation constant, $\{\beta^2(\omega), \mathbf{h}_t(\mathbf{x}_t, \omega)\}$. The modes corresponding to the scaled version of the system will satisfy the wave equation for the refractive index distribution,

$$n_s(\mathbf{x}_t, \omega) = n(\mathbf{x}_t/s, \omega), \quad (3.2)$$

where the subscript s identifies magnitudes of the scaled system (Pinheiro Ortega, 2008).

Based on the symmetry properties of Maxwell's equations, when the system involves only non-dispersive media, it is possible to establish a direct relationship between the modes corresponding to the original system and the scaled one (Joannopoulos et al., 2008). In order to develop a less restrictive framework, let us assume that the dispersive behavior of the refractive index distribution in the system differs from that of a certain reference material, $n_{\text{ref}}(\omega)$, by an amount that remains constant within the spectral bandwidth of interest (Pinheiro Ortega, 2008), i.e.,

$$\frac{\partial(n^2(\mathbf{x}_t, \omega) - n_{\text{ref}}^2(\omega))}{\partial\omega} \approx 0. \quad (3.3)$$

This hypothesis is valid for a large number of guiding systems, which provides a great help in our analysis in Chapters 4 and 5. For a conventional step index fiber, the silica cladding can be chosen as the reference, $n_{\text{ref}}(\omega)$. For those systems with nontrivial claddings — e.g., photonic crystal fibers — the refractive index of the solid core can be chosen as the reference. The successful application of the previous hypothesis to the design of photonic crystal fibers (Silvestre et al., 2006; Ferrando et al., 2001), reveals that the

results of this section are quite insensitive to not so small relative dispersion in the involved materials.

By subtracting the term $(\omega/c)^2 n_{\text{ref}}^2(\omega) \mathbf{h}_t$ from both sides of Equation 3.1 and taking into account the approximation in Equation 3.3, the wave equation can be rewritten as

$$\left[\nabla_t^2 + \left(\frac{\omega}{c} \right)^2 \Delta n^2(\mathbf{x}_t) \right] \mathbf{h}_t = \Delta \beta^2 \mathbf{h}_t, \quad (3.4)$$

where $\Delta \beta^2 = \beta^2 - (\omega/c)^2 n_{\text{ref}}^2(\omega)$. In this way, the elimination of the dispersive character of the term $\Delta n^2(\mathbf{x}_t) = n^2(\mathbf{x}_t, \omega) - n_{\text{ref}}^2(\omega)$ has been managed. Next, by applying a scaling transformation on Equation 3.4, defined by the change of variable $\mathbf{x}_t \mapsto \mathbf{x}_t/s$, and correspondingly $\nabla_t \mapsto s \nabla_t$, it leads to

$$\left[\nabla_t^2 + \left(\frac{\omega/s}{c} \right)^2 \Delta n^2(\mathbf{x}_t/s) \right] \mathbf{h}'_t = \frac{\Delta \beta^2}{s^2} \mathbf{h}'_t, \quad (3.5)$$

where $\mathbf{h}'_t(\mathbf{x}_t, \omega) = \mathbf{h}_t(\mathbf{x}_t/s, \omega)$.

Considering Equation 3.2 and defining a new working frequency of the scaling according to the transformation $\omega/s \mapsto \omega$, we get an equation of eigenvalues equivalent to Equation 3.4, but for a scaled system, given by

$$\left[\nabla_t^2 + \left(\frac{\omega}{c} \right)^2 \Delta n_s^2(\mathbf{x}_t) \right] \mathbf{h}_{ts} = \Delta \beta_s^2 \mathbf{h}_{ts}, \quad (3.6)$$

in which a solution has been identified corresponding to this scaled system, $\Delta \beta_s^2(\omega) = \Delta \beta^2(s\omega)/s^2$ and $\mathbf{h}_{ts}(\mathbf{x}_t, \omega) = \mathbf{h}_t(\mathbf{x}_t/s, s\omega)$.

The previous expression for the eigenvalue allows finding the relationship between the propagation constants of the scaled system and the original one, which can be simplified to

$$\beta_s^2(\omega) - \beta_{\text{ref}}^2(\omega) \approx \frac{1}{s^2} [\beta^2(s\omega) - \beta_{\text{ref}}^2(s\omega)], \quad (3.7)$$

where $\beta_{\text{ref}} = (\omega/c)n_{\text{ref}}$ is the propagation constant associated to the reference material.

By making two additional approximations on this equation, it is possible to get an approximate, simpler relationship between the propagation constants involved (Silvestre et al., 2006; Ferrando et al., 2001). According to the weak guiding approximation, we can assume that $\beta(\omega) \approx \beta_{\text{ref}}(\omega)$, and, in the same order of approximation, we can consider that the reference

propagation constant is weakly dispersive ($\beta_{\text{ref}}(s\omega) \approx s\beta_{\text{ref}}(\omega)$), in such a way that the following expression is reached (Pinheiro Ortega, 2008),

$$\beta_s(\omega) - \beta_{\text{ref}}(\omega) \approx \frac{1}{s}[\beta(s\omega) - \beta_{\text{ref}}(s\omega)]. \quad (3.8)$$

By deriving Equation 3.8 with respect to frequency once and twice, and carrying out the appropriate modifications, we obtain respectively the proper approximations for β_1 and β_2 ,

$$\beta_{1s}(\omega) \approx \beta_1(s\omega) - \beta_{1\text{ref}}(s\omega) + \beta_{1\text{ref}}(\omega), \quad (3.9)$$

$$\beta_{2s}(\omega) \approx s[\beta_2(s\omega) - \beta_{2\text{ref}}(s\omega)] + \beta_{2\text{ref}}(\omega), \quad (3.10)$$

in which they are referred to as the group index coefficient, β_1 , and the dispersion coefficient, β_2 . Once the $\beta(\omega)$, $\beta_1(\omega)$ and $\beta_2(\omega)$ functions are known for a specific guiding system within a given spectral range, Equations 3.8, 3.9 and 3.10 (or the more accurate Equation 3.7) will allow us to obtain a very good estimation of the dispersive behavior corresponding to any scaled version of that same system for the scaled spectral range, just recognizing the dispersion of a specific reference material. Additionally, these equations help us to find the appropriate value of the scale factor, s , that, when applied to the system, approaches either β , or one of its derivatives β_1 or β_2 , at a specific interest value or behavior for a given frequency ranges.

Later in this thesis project, Equation 3.8 will be a key starting point for us to derive formulas that help efficiently scale our guiding system using its parameters like the core radius and/or the core refractive index.

Chapter 4

Optical fiber profiling based on scaling symmetries and acousto-optic mode coupling

The usual way of describing an optical fiber is by the distribution of the refractive indices of its materials through the refractive index profile. The standard commercial optical fibers, like the SMF-28e, are considered to have a step index profile, in which the core and the cladding have piecewise constant refractive indices. That previous description works ideally when we solely consider the fundamental mode guided in the core. Nevertheless, when we have a broader look at the higher modes spreading outside of the core, it is significantly important to find an appropriate description and more realistic for the optical fiber refractive index profile, which ultimately helps having an accurate and proper fabrication process of the optical components.

In this chapter we show the process that has been followed to properly describe the fibers refractive index profile. Taking advantage of the experimental information provided by the mode couplings induced by the

acousto-optic interactions, and throughout iterative trials of fiber profile scaling and alteration, we will reach to more appropriate description of the refractive index profile.

4.1 Dispersion curves analysis

Acousto-optic interaction in optical fibers has been exploited as a technique to excite cladding modes which helps investigate the properties of optical fibers (Díez et al., 2000; Haakestad & Engan, 2006); it also controls the transmitted light in a way that is focused on coupling between the guided mode in the core and those modes guided by the cladding. This technique has been studied by the group of Fiber Optics (LFO) of the University of Valencia over the last decade (Cuadrado-Laborde et al., 2010; Alcusa-Sáez et al., 2014; Ramírez-Meléndez et al., 2016) for the accurate and broadband characterization of optical fibers and it has been exploited for developing dynamic and reconfigurable all-fiber devices.

From an experimental point of view, a piezoelectric transducer applied transversely to an optical fiber generates a flexural elastic waves on it. When these type of waves propagate along the optical fiber they create a traveling periodic refractive index perturbations which cause coupling between co-propagating optical modes.

As shown in Equation 2.31, for co-propagating mode coupling, maximum coupling between two modes is achieved at the optical wavelength at which the phase matching conditions are satisfied, i.e., when the acoustic resonance wavelength matches the beatlength between the two coupled optical modes (Saleh & Teich, 2001). The resonance wavelength, λ_R , is given by

$$\lambda_R = \Lambda \Delta n_{\text{eff}}. \quad (4.1)$$

On the other side, when the fiber is illuminated with the linearly polar-

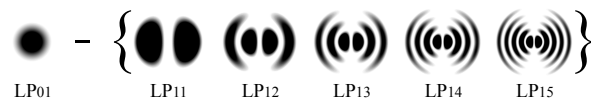


Figure 4.1: The modal distribution of the fundamental mode LP_{01} and the first five modes of the type LP_{1m} .

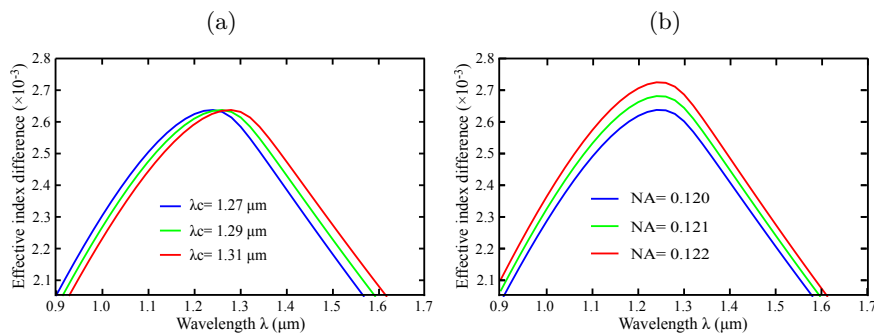


Figure 4.2: Simulated effective index difference curves, $\Delta n_{\text{eff}} = n_{\text{eff}}(\text{LP}_{01}) - n_{\text{eff}}(\text{LP}_{11})$, for two set of step index fibers. (a) Fibers with $\text{NA} = 0.120$ and different cutoff wavelengths, and (b) fibers with $1.28 \mu\text{m}$ cutoff wavelength and varying NA (Alcusa-Sáez et al., 2016).

ized (symmetric) fundamental mode, LP_{01} , the refractive index perturbation induced by the flexural acoustic waves favors its coupling with the LP modes that have an antisymmetric field distribution (LP_{1m} , $m = 1, 2, \dots$). Figure 4.1 shows the typical modal field distribution for the first fives modes of the LP_{1m} type alongside the fundamental mode, LP_{01} .

Recently, Alcusa-Sáez et al. (2016), with the aim of characterizing the propagating modes in optical fibers, have analyzed the experimental acousto-optic interactions and its related modal effective index difference and chromatic dispersion difference curves in SMF-28e and SM2000 fibers. Performing a series of numerical calculations they found that the effective index difference curve tends to shift regularly up, down, left and right by changing the core radius and the numerical aperture, i.e., the geometry and material of the core, which relate to the cutoff wavelength.

As shown in Figure 4.2(a), when the core radius increases at constant NA it means the cutoff wavelength will increase and the curve shifts to the right, while in Figure 4.2(b), when the numerical aperture increases while having a fixed cutoff wavelength the curve regularly shifts up (Alcusa-Sáez et al., 2016).

After a number of trials, they obtained fiber configurations that globally best describe their experimental results. For the SMF-28e fiber, the best fit corresponds with a cutoff wavelength, λ_c , of $1.40 \mu\text{m}$, a core radius, a ,

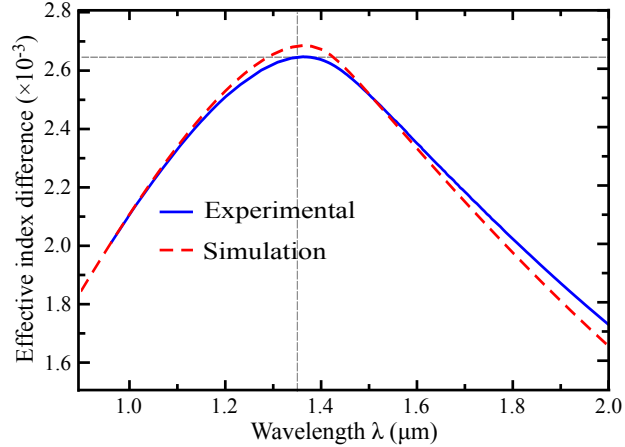


Figure 4.3: The effective index difference curve, $\Delta n_{\text{eff}} = n_{\text{eff}}(\text{LP}_{01}) - n_{\text{eff}}(\text{LP}_{11})$, measured experimentally (solid blue curve) and the simulated one (dashed red curve) from [Alcusa-Sáez et al. \(2016\)](#)

of $4.4287 \mu\text{m}$ and a numerical aperture, NA, of 0.121. In Figure 4.3 we can see that, even though the simulated curve and the experimental one are structurally similar, some mismatch is evident. In the next sections we analyze the cause of this mismatch and present an alternative model for the refractive index profile.

The dispersion curves of the fiber modes in this research have been computed using the Fourier based modal technique ([Silvestre et al., 2005](#)) previously explained in Section 2.2. This technique can compute the modes of optical fibers with arbitrary refractive index profile, which is the case of the analysis in this chapter.

In addition, considering the importance of material dispersion when simulating the chromatic dispersion correctly, we take into account the dispersion of pure silica by using the Sellmeier coefficients reported by [Fleming \(1984\)](#). Hence, the refractive index of the cladding material is accurately included in the calculations. The core refractive index was assigned by increasing the refractive index of the cladding by a constant value related to the numerical aperture. Alternatively, we evaluate the Germanium (Ge) concentration in the core with the numerical aperture value, using an interpolation taking into account the Sellmeier coefficients for a specific Ge

concentration, which ultimately gives the same results as before (Tashtush et al., 2019).

4.2 Controlling the core refractive index profile

Analyzing an optical fiber with a step index model requires two parameters to define the refractive index profile: the refractive index difference, $\Delta n = n_{\text{core}} - n_{\text{cladding}}$, and the core radius, a . Nonetheless, experimentally speaking, it is more common to have information on the numerical aperture and the cutoff wavelength of the first higher order mode, LP₁₁ (see Equation 2.14).

Taking into account the effect of the two parameters on dispersion curves shown in Figure 4.2, a convenient manner for attempting to fit the experimental dispersion curve and the simulated one is trying to match a common characteristic feature as it is the local maximum appearing near the cutoff wavelength, characterized by the maximum value of Δn_{eff} , $\Delta n_{\text{eff,max}}$, at the corresponding wavelength, λ_{max} .

The behavior shown in Figure 4.2(a) can be reviewed using the concept of scaling, which was explained in the previous chapter. By using the relation between the propagation constant and the effective index for a given mode, where $\beta(\omega) = (\omega/c)n_{\text{eff}}(\omega)$, we can rewrite Equation 3.8, which describes the approximation for the propagation constant for a scaled system as

$$n_{\text{eff},s}(\omega) - n_{\text{ref}}(\omega) \approx n_{\text{eff}}(s\omega) - n_{\text{ref}}(s\omega), \quad (4.2)$$

where $n_{\text{eff},s}(\omega)$ is the effective index of the mode at issue of the scaled structure at frequency ω , and $n_{\text{ref}}(\omega)$ is the effective index of a reference material at frequency ω . Next, subtracting Equation 4.2 for two different modes, and expressing it in terms of wavelength, will lead to

$$\Delta n_{\text{eff},s}(\lambda) \approx \Delta n_{\text{eff}}\left(\frac{\lambda}{s}\right). \quad (4.3)$$

This implies that the effective index difference of a scaled system at a specific wavelength approximately equals the effective index difference of the initial system at a wavelength of λ/s where s is the magnitude of the scale factor.

Using the same concept on Equations 3.9 and 3.10, which represent the first and the second derivatives of β respectively, the group index difference and dispersion difference can be expressed by

$$\Delta n_{g,s}(\lambda) \approx \Delta n_g \left(\frac{\lambda}{s} \right), \quad (4.4)$$

and

$$\Delta D_s(\lambda) \approx \frac{1}{s} \Delta D \left(\frac{\lambda}{s} \right), \quad (4.5)$$

where $\Delta n_{g,s}(\lambda)$ and $\Delta D_s(\lambda)$ are, respectively, the group index difference and the dispersion difference of the scaled system.

The effective index difference curves behavior shown in Figure 4.2(a) can give us the opportunity to estimate the scale factor. This factor will play an essential role in shifting the effective index curve as desired. Accordingly, to match the simulated curves and the experimental ones, first, we must determine the scaling transformation that shifts the maximum wavelengths of the simulated curve to the maximum wavelength of the experimental curve [labeled respectively as ‘(sim)’ and ‘(exp)’]. That scale factor, M , can be estimated as the ratio between the wavelengths at which $\Delta n_{\text{eff}}^{(\text{exp})}$ and $\Delta n_{\text{eff}}^{(\text{sim})}$ (the previously simulated structure) are maximum,

$$M = \frac{\lambda_{\text{max}}^{(\text{exp})}}{\lambda_{\text{max}}^{(\text{sim})}}. \quad (4.6)$$

M is referred to as the core radius scale factor.

Moreover, as it has been shown from the definition of the V parameter (Equation 2.13), it is apparent that the relation between the numerical aperture and the radius is linear if we kept in mind maintaining the V value fixed, which approximately preserves the fiber propagation constants. Looking back at Figure 4.2(b), the curves vertical shift will be helpful for us to define another scale factor, which parametrize the scaling in refractive index difference, $\Delta n^2 = n_{\text{core}}^2 - n_{\text{cladding}}^2$. In the next equation it is shown how the new scale factor is estimated through a proportionality relation, which can be described as

$$N = \frac{\Delta n_{\text{eff,max}}^{(\text{exp})}}{\Delta n_{\text{eff,max}}^{(\text{sim})}}, \quad (4.7)$$

where $\Delta n_{\text{eff,max}}^{(\text{exp})}$ is the maximum value on the experimental effective index difference curve, $\Delta n_{\text{eff,max}}^{(\text{sim})}$ is the maximum value on the simulated effective index difference curve, and N is to be called the refractive index scale factor.

It is significant to realize that this process can be iterated and the preset reference maximum point on the simulated curve, $\Delta n_{\text{eff}}^{(\text{sim})}$, changes with each iteration, which in fact helps producing more accurate results.

After using Equations 4.6 and 4.7 to estimate the refractive index scale factor, N , and the core radius scale factor, M , and bearing in mind the cross effect of M and N in the optical volume of the core, we can calculate the new scaled optical fiber refractive index profile as

$$a = \frac{Ma_0}{\sqrt{N}}, \quad (4.8)$$

$$\Delta n^2 = N\Delta n_0^2, \quad (4.9)$$

where a and a_0 are, respectively, the core radius after and before scaling, and Δn^2 and Δn_0^2 are, respectively, the core refractive index difference after and before scaling.

The new values of the core radius and the refractive index contrast provided by the last two formulas define a new fiber configuration to be simulated and its results can be taken as a new starting point at which to apply Equations 4.6 to 4.9. After few iterations, this procedure adjusts the effective index difference curve to the preset reference point on the experimental curve, which in our case is the point where the index difference curves are maximum.

In Figure 4.4 it is noticeable how the curve is adjusted to overlap the experimental one showing what we consider the best fit to a step index model. This fit was obtained after adjusting the fiber parameters in order to match the maximum points on the dispersion difference curves. The figure shows a perfect fit in the region below the cutoff wavelength, i.e., when both LP_{01} and LP_{11} modes are guided in the core of the fiber ($\lambda < \lambda_c \approx 1.4 \mu\text{m}$), but we still have a noticeable mismatch in the region where the second guided mode is above cutoff. We found that the best fitting values for the core radius, cutoff wavelength and numerical aperture were, respectively, $a = 4.415 \mu\text{m}$, $\lambda_c = 1.385 \mu\text{m}$ and $\text{NA} = 0.1201$. In this wavelength range, we consider that the refractive index profile within the core should dominate the dispersion difference between the two modes.

As it has been noticed from the last results, even after rescaling the core, the simulated standard single mode fiber refractive index still does not have the proper description when it is compared with the experimental results. Therefore, a modification on the ideal model of the single mode fiber has to be performed.

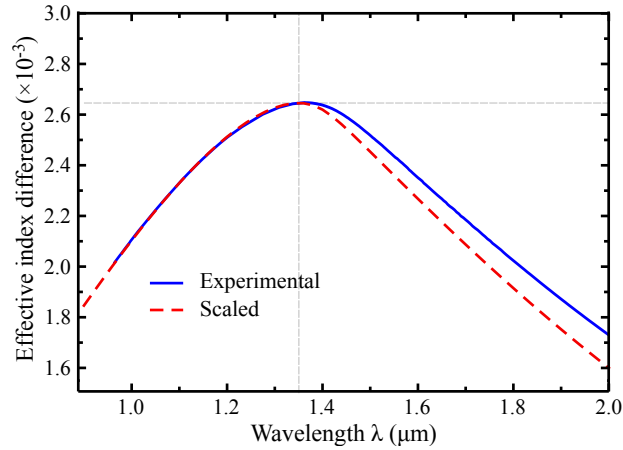


Figure 4.4: The modal index difference $\Delta n_{\text{eff}} = n_{\text{eff}}(\text{LP}_{01}) - n_{\text{eff}}(\text{LP}_{11})$ for the experimental curve (solid blue curve) and the scaled simulated (dashed red curve) optical fiber profile.

Many publications have profoundly described the real refractive index profile of the fiber. One of these intensive more realistic profiles, like the one described in Figure 4.5 (Abrishamian et al., 2012), follows many irregularities and perturbations in the cladding and a smooth stooping behavior in the core with a small dip in the center. The figure shows the refractive index profile of the fiber before and after being discharged with a specific amount of electric current; this whole process is meant to show how the profile changes due to the discharge, but for our research proposes we needed to look at the curve of the original fiber (solid blue curve).

We realized that there are two possibilities to change the ideal refractive index profile structure into more realistic one. On the one hand we can modify the core material by creating an index change, whether on the sides of the core, as described by Olshansky & Keck (1976), and/or by creating a central dip and reduction on the refractive index material in the core center, as described by Gambling et al. (1977). On the other hand, we can go further and change the refractive index of the cladding. These steps are possible using the concept of power law index.

The power law index is a function that defines the material distribution of the fiber in an inhomogeneous way and depends mainly on two variables

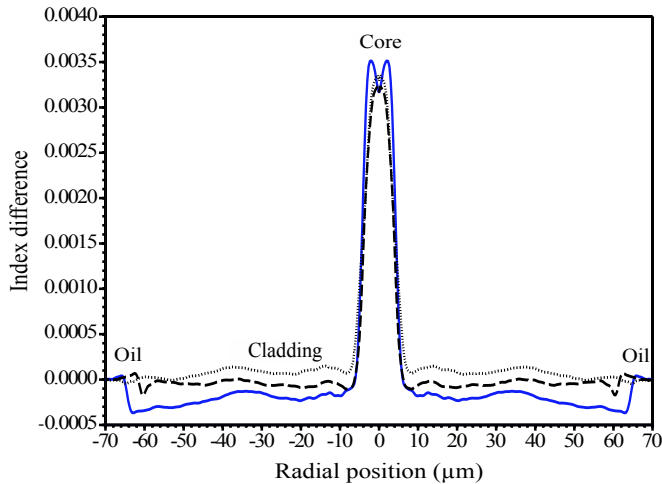


Figure 4.5: The original refractive index profile of a SMF-28e fiber (solid blue curve), from [Abrishamian et al. \(2012\)](#).

characterizing the spatial dependence: $\alpha \geq 0$, which controls the central dip, and $\beta \geq 1$, which controls the profile around the core-cladding interface. In summary, the next function has been used to model the core refractive index profile,

$$n^2(r) - n_{\text{cladding}}^2 \propto (r/a)^\alpha [1 - (r/a)^\beta], \quad r \leq a, \quad (4.10)$$

where α and β are the power law index parameters, a is the core radius and n_{cladding} is the cladding refractive index.

Figure 4.6 shows how the fiber core refractive index profile changes when the values of α [Figure 4.6(a)] and β [Figure 4.6(b)] are modified, keeping in mind that the standard fiber with step index model has a power law index parameters of $\alpha = 0$ and $\beta = \infty$ [see dashed black curves in Figures 4.6(a) and (b)].

Performing the previous analysis on the core shows that no significant improvement can be reached by adjusting the core profile. In fact, the change creates an extra mismatch on the curve where $\lambda < \lambda_c \approx 1.4 \mu\text{m}$. By going back to Figure 4.4, it is noticeable that the best fit we have got aligns perfectly on the left side of the curve which describes the region below cutoff ($\lambda < \lambda_c \approx 1.4 \mu\text{m}$) but it is not the case on the right side (above cutoff wavelength).

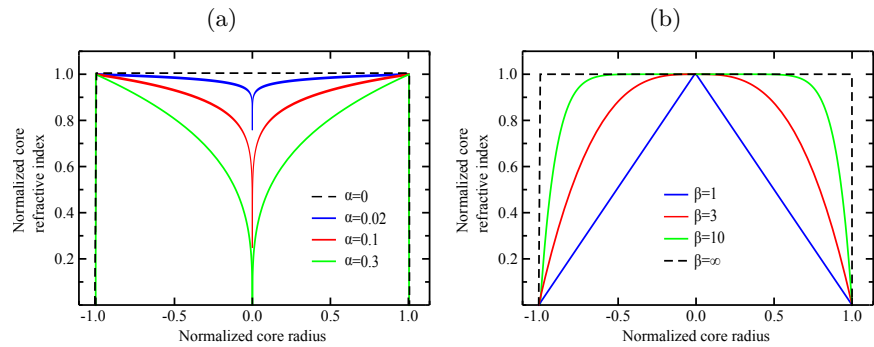


Figure 4.6: The fiber core profile changes when (a) the parameter α changes adding a central dip (for $\beta = \infty$), and (b) the parameter β change modifying the outer structure (for $\alpha = 0$).

After realizing that any refractive index variation following a realistic profile in the core, as that described by [Abrishamian et al. \(2012\)](#), gave no significant deviation with respect to the measured points, we had to consider a refractive index perturbation that modifies the dispersion of the cladding mode, but preserves the dispersion of the fundamental mode. In fact, the experimental measurement of the cladding refractive index reported by [Abrishamian et al. \(2012\)](#) and presented in Figure 4.5 shows that type of fluctuations and irregularity in the refractive index profile of the cladding.

4.3 Controlling the cladding refractive index profile

The previous section shows that we could simulate a dispersion curve with a very good fit with the experimental one only below the cutoff wavelength, and we always found that the theoretical refractive index difference above cutoff ($\lambda > \lambda_c \approx 1.4 \mu\text{m}$) was somewhat underestimated, which calls for altering the ideal model of the cladding. As it was mentioned at the beginning of this chapter, the optical fiber refractive index profile has a significant importance in describing the fiber manufacturing material distribution and the signs of any stress, strain or deformation that the fiber suffers.

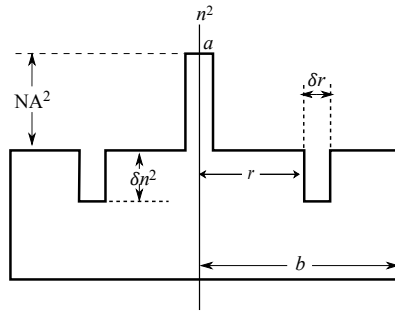


Figure 4.7: The new fiber refractive index profile after adding a perturbation in the cladding.

For simplicity and to have an early understanding on the dispersion curves behavior when a refractive index change happens in the cladding, we considered a refractive index perturbation defined by a ring with inner radius r , a width of δr , and a refractive index drop of δn , compatible with the average cladding fluctuations described by [Abrishamian et al. \(2012\)](#). Figure 4.7 shows the simulated fiber profile after introducing the ring in the cladding refractive index. The best fitting values were $r = 30 \mu\text{m}$, $\delta r = 10 \mu\text{m}$, and $\delta n = 4.5 \times 10^{-4}$ with respect to the cladding silica refractive index at $1.55 \mu\text{m}$.

Figure 4.8 shows the change occurred on the effective index difference curve before, see Figure 4.8(a), and after, see Figure 4.8(b), adding this type of refractive index perturbation in the cladding. Figure 4.8(a) shows how there was a mismatch between the experimental results (solid blue curve) and the simulated ones (dashed red curve), while Figure 4.8(b) shows a really good fit of the effective index difference $[n_{\text{eff}}(\text{LP}_{01}) - n_{\text{eff}}(\text{LP}_{11})]$ curve between the experimental (solid blue curve) and simulation (dashed red curve) after we add the described cladding perturbation. This new atypical yet simple fiber profile has given us a closer look on the further possible simulations and theoretical solutions for an unconventional model of fiber profiles.

A merit function, χ , has been defined to measure the root mean square value of the mismatch in the effective index difference and it can be described

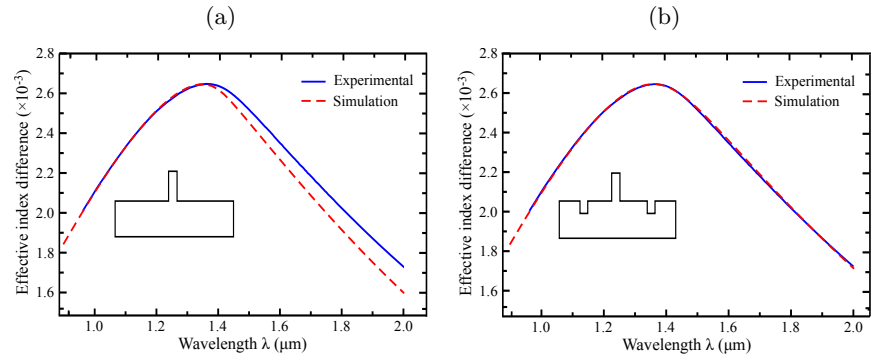


Figure 4.8: The simulated effective index difference curve of LP₀₁–LP₁₁ (dashed red curve) and the experimental one (solid blue curve) for (a) the original fiber with no change on the refractive index profile, and (b) when the ring perturbation is added in the cladding refractive index.

as

$$\chi^2 = \frac{1}{K} \sum_{q=1}^K [\Delta n_{\text{eff}}^{(\text{sim})}(\lambda_q) - \Delta n_{\text{eff}}^{(\text{exp})}(\lambda_q)]^2, \quad (4.11)$$

where K refers to the number of selected wavelengths, $\Delta n_{\text{eff}}^{(\text{sim})}(\lambda_q)$ and $\Delta n_{\text{eff}}^{(\text{exp})}(\lambda_q)$ are respectively, the simulated effective index difference at the wavelength λ_q and the experimental effective index difference at the same wavelength. The results show that, with the previous perturbation added in the cladding, χ is around 1.4×10^{-3} , which display an effective index difference mismatch improvement of three times better than what was presented in [Alcusa-Sáez et al. \(2016\)](#) modeling.

As mentioned at the beginning of the chapter, beside the effective index difference curve, the group index difference and the dispersion difference curves are also used for characterizing few mode fibers. All three of these curves are connected through derivations with respect to frequency, which means to demand even more accurate fitting processes, and, correspondingly, we ought to check the effect of the new refractive index profile on these curves. For simplicity, we will check the second order derivative curve, the dispersion difference.

Unfortunately, while a fiber with the previously described refractive in-

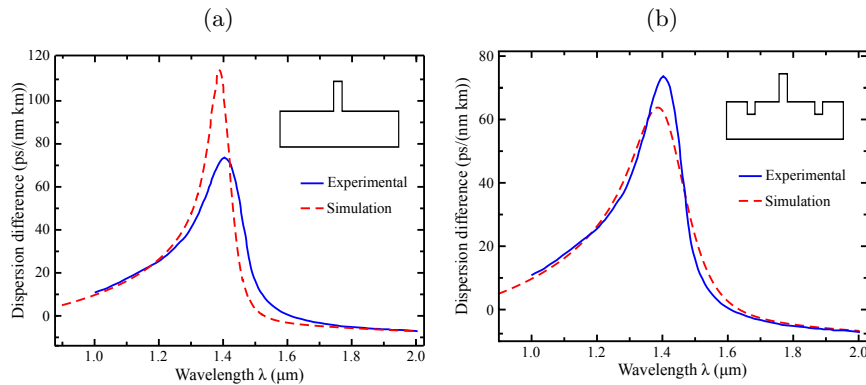


Figure 4.9: The simulated dispersion difference curves (dashed red curve) compared to the experimental (solid blue curve) for an optical fiber (a) with an ideal refractive index profile, and (b) a fiber profile with a perturbation ring in the cladding refractive index.

dex profile (with a ring in the cladding) fits the experimental effective index difference curve, it still has a noticeable relative error when it comes to the dispersion difference curve as shown in Figure 4.9(b). The figure shows how the dispersion difference curve improved significantly from the case where the ring is not present, Figure 4.9(a), to the case where it is, Figure 4.9(b), although still not desirably fitted.

An alternative and possibly less trivial description had to be found. As in our calculations the material chromatic dispersion has been included (Fleming, 1984), we took into account the cladding perturbation reported by Violakis et al. (2012). At this point, it is beneficial to use the concept of power law index to describe that perturbation in the cladding. Instead of a simple constant drop in the refractive index, we can describe these perturbation as a steady linear decline in the refractive index, as shown in Figure 4.10, knowing that this step is achievable by having a cladding with $\alpha = 0$ and $\beta = 1$ (see Equation 4.10). This approach would help spread the perturbation effect along the cladding, which will presumably give a fiber refractive index profile closer to the realistic one.

We assumed this physical perturbation of refractive index is originated, according to Violakis et al. (2012), by the induced differential stress between the core and the outer surface of the fiber during the drawing process.

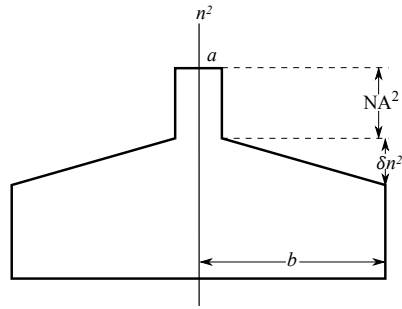


Figure 4.10: The refractive index profile introducing a linear decline in the cladding refractive index.

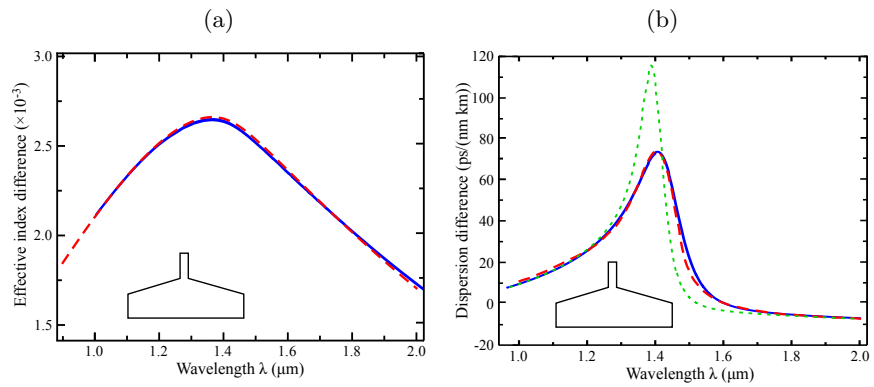


Figure 4.11: (a) The simulated effective index difference curve for the fiber profile with perturbed cladding [see inset] (dashed red curve) fitting the experimental one (solid blue curve). (b) The simulated dispersion difference curve for the same profile in the inset (dashed red curve) fitting the experimental one (solid blue curve), both compared to the fiber where no perturbation is added (dotted green curve).

Typically, the value for such stress difference is 20 MPa, and therefore the expected refractive index difference, δn , would be around 1.3×10^{-4} [taking the extraordinary and ordinary photoelastic constants of silica equals to 5.5×10^{-13} and $4.22 \times 10^{-12} \text{ m}^2/\text{N}$, respectively (Primak & Post, 1959)].

This perturbation, described as a decline in the cladding refractive index,

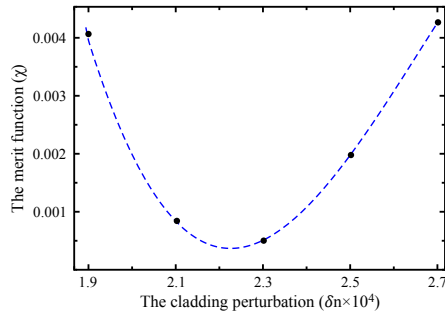


Figure 4.12: The value of χ with respect to the refractive index perturbation δn . The dashed blue line is an interpolation of the simulated values (black dots).

can be modeled with a single parameter, δn , which in our analysis, and after few trials, turned out to equal 2.3×10^{-4} with respect to the cladding silica refractive index at $1.55 \mu\text{m}$. By using this parameter in combination with a step index profile for the fiber core, we obtain a very good match between theory and experiment, as shown in Figure 4.11(a) and Figure 4.11(b), which respectively, present the best fitted results for the effective index difference and the dispersion difference for (LP_{01} – LP_{11}). Moreover, by going back to the previously defined merit function, we found that χ value becomes 5.1×10^{-4} , which means comparing to the previous cladding perturbation design, the effective index difference mismatch of this new refractive index profile design with the experimental one is almost three times lower.

The value of this linearly declining refractive index change in the cladding, δn , has been manipulated and tested through the previously mentioned merit function to retrieve the best value for the best fitting. Figure 4.12 shows the variant values of cladding perturbation we used versus their corresponding mismatch merit function value, χ .

As presented in our analysis, this whole fitting process is performed first on an SMF-28e fiber. Therefore, to confirm the effectiveness of these last results, we performed the same fitting process on the other commercial fiber, SM2000, analyzed by [Alcusa-Sáez et al. \(2016\)](#), with best-fit values of $5.380 \mu\text{m}$ core radius, a cutoff wavelength of $1.657 \mu\text{m}$, and 0.1180 numerical aperture. Figures 4.13(a) and 4.13(b), respectively, show how the simulation have a good fit with the experimental results for both effective index and dispersion differences when a perturbation of $\delta n = 3.8 \times 10^{-4}$ (see Figure

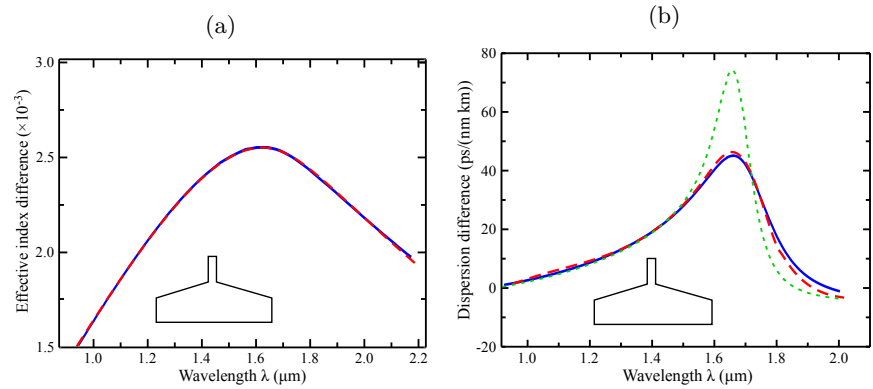


Figure 4.13: The SM-2000 fiber results. (a) The simulated effective index difference curve for the new (inset) fiber profile (dashed red curve) fitting the experimental one (solid blue curve). (b) The simulated dispersion difference curve (dashed red curve) for the same profile fitting the experimental (solid blue curve), both compared to the fiber where no perturbation is added (dotted green curve).

4.10) is considered in the cladding. As for the mismatch, χ value, of the effective index difference curve, calculated for this type of fiber, it shows an improvement of almost 10 times in the effective index difference fit with a χ value dropping from 1.6×10^{-3} to 1.7×10^{-4} when the last perturbation is introduced.

4.4 Fitting high order dispersion curves

In the previous section, we presented two methods where a perturbation is introduced in the cladding, which help describing a proper realistic optical fiber refractive index profile. These methods have been expressed plainly through the effective index difference curve between the fundamental mode and the first higher mode, i.e, LP_{01} - LP_{11} . As the fundamental mode, LP_{01} , mostly passes through the core and that is the case for the first high order mode, LP_{11} , when below cutoff, the curves are somewhat meant to match. However as the LP_{11} mode starts to pass through the cladding ($\lambda > \lambda_c$), any type of perturbation will affect the effective index of the mode. Since in both previous cases the modification in the fiber happens in the cladding

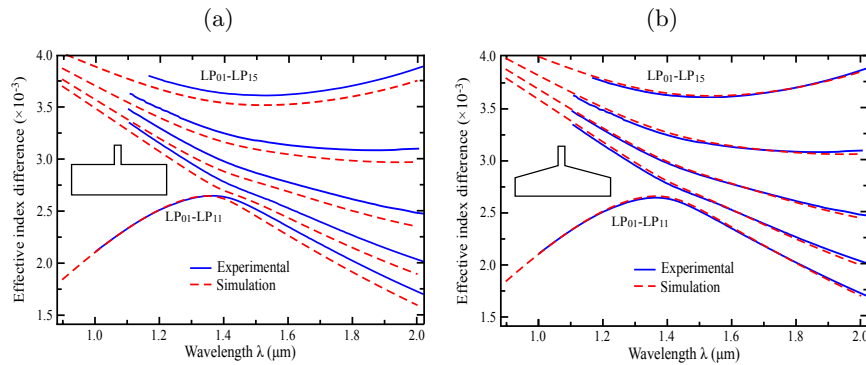


Figure 4.14: The simulated effective index difference curves between the LP_{01} and the LP_{11} , LP_{12} , LP_{13} , LP_{14} and LP_{15} modes compared to the experimental ones for the SMF28-e fiber before (a) and after (b) adding a perturbation in the cladding.

so it is a necessity to check the compatibility of the other higher modes of the order $(1, m)$.

Figure 4.14(a) shows that when we have a standard optical fiber with a step index refractive index profile, the experimental effective index differences between the mode LP_{01} and the higher modes LP_{11} to LP_{15} do not have a good fit with the simulated ones. On the other hand, Figure 4.14(b) shows the effect of introducing the recently defined perturbation in the cladding (inset) on the index differences curves, which result a quite good fit for all of these modes. Figure 4.14(b) also shows that this new perturbation in the cladding affect significantly the higher order coupled modes, LP_{12} , LP_{13} , LP_{14} , and LP_{15} , on a noticeable level over the whole wavelength range, above and below cutoff.

This concludes that as the higher modes are considered over long wavelength ranges they spread more and are affected not just of the structure and material homogeneity of the core but also of what occurs in the cladding.

The focus on the cladding inhomogeneity, which helped reaching a fiber profile effective index difference fits the experimental one for the index difference between modes LP_{01} and LP_{11} , paved the way to study the curves behavior of the other higher modes of the order LP_{1m} . Revising the higher order modes behavior gives a better and conclusive refractive index profile

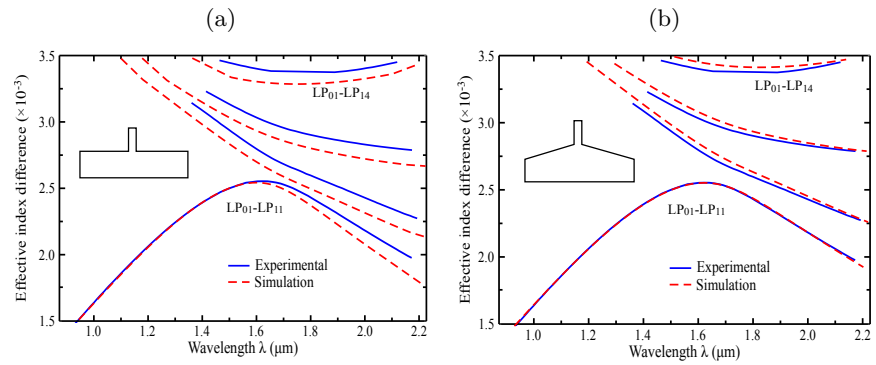


Figure 4.15: The simulated effective index difference curves between the LP_{01} and the LP_{11} , LP_{12} , LP_{13} and LP_{14} modes compared to the experimental ones for the SM-2000 fiber before (a) and after (b) adding a perturbation in the cladding.

description of the optical fiber. Correspondingly, we have managed to reach a fiber refractive index profile design, which is more realistic and coincides with the experimentally measured mode couplings. Again, it is worth keeping in mind, that the final attained parameters related to the optical fiber are a result of few iterative simulations. Applying the same process on the SM-2000 fiber we found that also the results for the higher coupled modes got a better fit than when the cladding has no perturbation as it is shown in Figure 4.15.

This once more proves that the final introduced approach, by presenting improvement on the effective index curves, is in fact comprehensive and could be applied for a wide range of commercial standard fibers, which solidify the case on the previously introduced perturbation in the cladding refractive index.

Chapter 5

Optical fiber profiling based on scaling symmetries and inscribed Bragg gratings modes coupling

In the previous chapter, we studied how the mode couplings caused by acousto-optic perturbations can help us identify the stress effect on the fiber refractive index profile, which leads us into a more realistic representation for the optical fiber. In this chapter, we continue with the analysis of the fiber refractive index profile using the mode couplings triggered by permanently inscribed Bragg gratings.

This approach is different than what was presented before as the perturbation in the refractive index caused by acoustic waves is usually small (Snyder & Love, 1983; Alcusa-Sáez, 2017) and dynamically adjustable. In fact, the analysis in this chapter will give us a solid confirmation on the approach we presented previously to characterize the cladding refractive index in the presence of the stress effect. It is also noted that the wavelength range will not be as wide as before ($1\ \mu\text{m}$) but over a few tens of nanometers which will provide a closer intense look at the coupling resonances.

5.1 Fiber profile scaling and dispersion curves

To deal with the fiber profiling in the case of UV-photo inscribed Bragg gratings, we need to extend the scaling analysis depicted in Chapter 3 to describe more accurately the core refractive index scaling together with the geometry scaling (see Section 4.2).

We start with the approximate Equation 3.4,

$$\left[\nabla_t^2 + \frac{\omega^2}{c^2} \Delta n^2(\mathbf{x}_t) \right] \mathbf{h}_t(\mathbf{x}_t, \omega) \approx \Delta \beta^2(\omega) \mathbf{h}_t(\mathbf{x}_t, \omega), \quad (5.1)$$

where $\Delta \beta^2 = \beta^2 - (\omega/c)^2 n_{\text{ref}}^2(\omega)$ and $n_{\text{ref}}(\omega)$ is the refractive index of a known reference under the assumption given by Equation 3.3 [the dispersive behavior of the distribution of the refractive index of the system differs from a certain reference material, $n_{\text{ref}}(\omega)$, in a nearly constant amount].

Next, by applying a scaling transformation to the refractive index difference, $\Delta n^2(\mathbf{x}_t) \mapsto \Delta n_{[N]}^2(\mathbf{x}_t) = N \Delta n^2(\mathbf{x}_t)$ and an inverse scaling to the angular frequency, $\omega^2 \mapsto \omega_N^2 = \omega^2/N$, we obtain an equation structurally equal to Equation 5.1 just identifying the eigenfunctions and eigenvalues of both equations, $\mathbf{h}_{t,[N]}(\mathbf{x}_t, \omega_N) = \mathbf{h}_t(\mathbf{x}_t, \omega)$ and $\Delta \beta_{[N]}^2(\omega_N) = \Delta \beta^2(\omega)$. From the last equation, we get the expression for the effective index difference when the fiber refractive index difference is scaled:

$$\Delta n_{\text{eff},[N]}^2(\omega) \approx N \Delta n_{\text{eff}}^2(\sqrt{N}\omega). \quad (5.2)$$

Considering the cladding material as the reference material, $n_{\text{ref}}(\omega) = n_{\text{clad}}(\omega)$, we can estimate the effective index in a fiber with scaled refractive index difference as

$$n_{\text{eff},[N]}^2(\omega) \approx N \left[n_{\text{eff}}^2(\sqrt{N}\omega) - n_{\text{clad}}^2(\sqrt{N}\omega) \right] + n_{\text{clad}}^2(\omega), \quad (5.3)$$

where $n_{\text{eff}}(\omega)$ is the effective index of a guided mode in the unscaled refractive index difference distribution at the frequency ω and N is referred to as the refractive index difference scale factor.

In Chapter 3 (and Section 4.2) we have obtained a similar relationship when the geometry is scaled (see Equation 3.7 and 4.2); by taking in this scaling the core index, n_{core} , as our reference, we can calculate the effective index in a fiber with scaled geometry, $n_{\text{eff},M}(\omega)$, at a frequency ω , as

$$n_{\text{eff},M}^2(\omega) \approx n_{\text{eff}}^2(M\omega) - n_{\text{core}}^2(M\omega) + n_{\text{core}}^2(\omega), \quad (5.4)$$

where again $n_{\text{eff}}(\omega)$ is the effective index of a guided mode in the geometrically unscaled distribution at the frequency ω and M is the geometry scale factor.

Applying successively both scaling Equations 5.3 and 5.4, we obtain a comprehensive formula that estimate the effective index difference of a guided mode in fiber with scaled geometry and refractive index difference distribution, $n_{\text{eff},M[N]}^2(\lambda)$, at any wavelength, i.e.,

$$n_{\text{eff},M[N]}^2(\lambda) = N \left[n_{\text{eff}}^2 \left(\frac{\lambda}{M\sqrt{N}} \right) - n_{\text{clad}}^2 \left(\frac{\lambda}{M\sqrt{N}} \right) \right] + n_{\text{clad}}^2(\lambda). \quad (5.5)$$

5.2 Refractive index profile scaling for a BG

As explained in Section 2.4, periodic perturbations in fibers stimulate the power transfer from the illumination mode to other modes, in such way that notches appear in the transmission spectrum at the resonance wavelengths. In the case of fiber Bragg gratings, the cylindrical symmetry of the perturbation favors the coupling between modes with the same symmetries, and therefore mode HE_{11} couples to modes HE_{1m} . The resonance wavelengths depend, as shown before, on the effective modal indices of the two coupled modes, which depends on the properties of the fiber, and on the Bragg grating period (see Equation 2.31).

Figure 5.1 shows the transmission spectrum for a Bragg grating with a period, Λ , of 533.5 nm, written in a fiber used experimentally by [Poveda-Wong et al. \(2017\)](#), where the fiber is of the type SM1500 with NA of 0.29, a cutoff wavelength of 1.387 μm and a modal field diameter of 4.2 μm .

It is noticeable how the depth of these notches, which is referred to as the coupling efficiency, is different for each mode coupling. This has its origin in the coupling coefficient of each resonance [see [Kitayama & Ikeda \(1978\)](#); [Savovic & Djordjevich \(2007\)](#) for more about the calculations of coupling coefficient].

In the same figure, the core mode HE_{11} resonance wavelength is easily detectable at 1556.9 nm, with a depth that exceeds -38 dB. The other resonances relate to the couplings with the cladding modes. The main set of resonances have a depth of approximately -1.5 dB around 1540 nm, this set refers to the cladding modes HE_{1m} and EH_{1m} ([Yin et al., 2013](#)). The second set of resonances, which have notch depth around -0.1 dB, are associated with the modes TE_{0m} , TM_{0m} and HE_{2m} ([Thomas et al., 2011, 2012](#)).

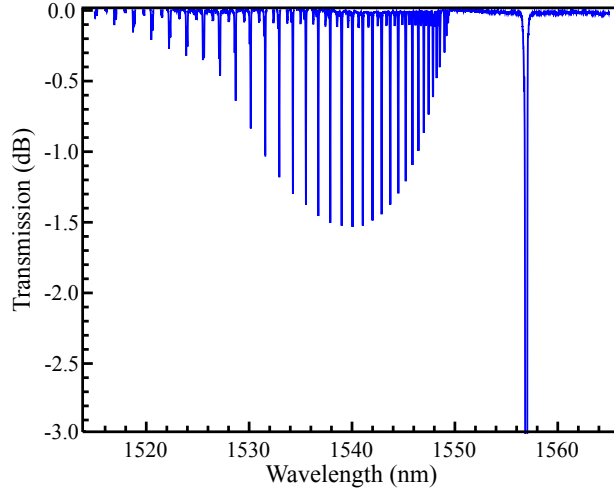


Figure 5.1: Transmission spectrum for a Bragg grating (Poveda-Wong et al., 2017).

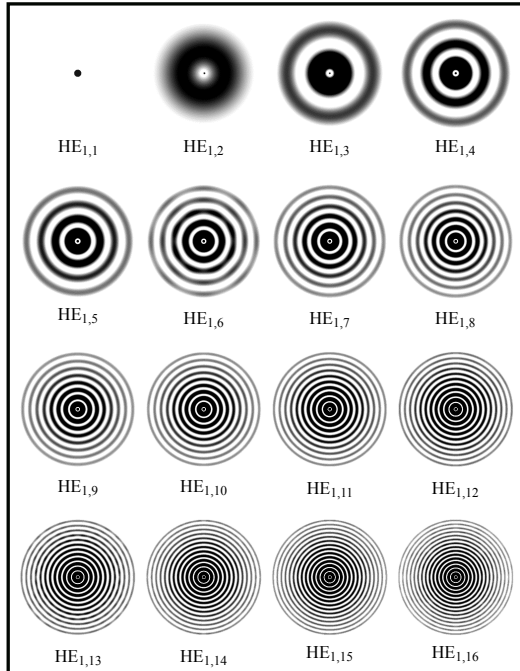
Identifying these HE_{1m} modes through their modal field distribution is reasonably easy even for high orders as m goes to few tens. Table 5.1 shows the modal distribution for the first 16 modes of the type HE_{1m} .

Regarding the main set of resonances, the coupling with the EH_{1m} modes around 1520 nm is stronger than it is with the HE_{1m} , while the coupling with HE_{1m} modes become more recognizable around the 1540 nm and the EH_{1m} modes notches are almost zero. As for the mode couplings around the high wavelength ranges (1545 nm – 1550 nm), they are not easily identifiable. Additionally as we go further in our analysis, it is apparent that the estimated effective index at the experimental resonance wavelengths would not quite fit the simulated effective index curves on such a small wavelength range. Hence, we had to find a proper way to identify these resonances and then scale the fiber refractive index profile to have a better fitting results.

In order to develop a fiber profiling strategy, we can start particularizing the Bragg conditions, expressed by Equation 2.32, for the case in which the illumination mode ('0') couples with itself but propagating in the opposite direction, and for the case of coupling to other counter-propagating modes (' μ ')

$$\lambda_{R,0} = 2n_0(\lambda_{R,0})\Lambda,$$

Table 5.1: The usual modal distribution for the modes of the type HE_{1m} in a step index fiber.



$$\lambda_{R,\mu} = [n_0(\lambda_{R,\mu}) + n_\mu(\lambda_{R,\mu})]\Lambda,$$

where $n_0(\lambda)$ and $n_\mu(\lambda)$ are the effective refractive indices of the considered modes and $\lambda_{R,0}$ and $\lambda_{R,\mu}$ are the corresponding resonance wavelengths predicted by the Bragg condition. [For lightening notation hereinafter the subscript ‘eff’ is being removed from the effective refractive index variables.]

Combining these two last equations we can obtain a new expression bounding indices and resonance wavelengths,

$$n_\mu(\lambda_{R,\mu}) = 2n_0(\lambda_{R,0}) \frac{\lambda_{R,\mu}}{\lambda_{R,0}} - n_0(\lambda_{R,\mu}). \quad (5.6)$$

It is worth stressing that this equation will only be satisfied if $n_0(\lambda)$ and $n_\mu(\lambda)$ describe accurately the modes of the fiber exhibiting the resonances $\lambda_{R,0}$ and $\lambda_{R,\mu}$, i.e., it can be used as a test of the goodness of the fiber

profile description. Specifically, we can define a merit function as a root mean square of the mismatch given by Equation 5.6 for a series of modes and resonances,

$$\chi^2 = \frac{1}{K} \sum_{\mu=1}^K \left[2n_0(\lambda_{R,0}) \frac{\lambda_{R,\mu}}{\lambda_{R,0}} - n_0(\lambda_{R,\mu}) - n_\mu(\lambda_{R,\mu}) \right]^2, \quad (5.7)$$

where K is the number of coupled modes considered. Now, to ease the process of testing fiber configurations against the merit function χ , it is convenient to use Equation 5.5 for estimating the dispersion relation of a family of scaled fibers based on a given configuration. In addition, as the illumination mode will be more sensitive to the scaling transformations it is sufficient to apply the scaling to that mode:

$$\chi_{M,[N]}^2 = \frac{1}{K} \sum_{\mu=1}^K \left[2n_{0,M[N]}(\lambda_{R,0}) \frac{\lambda_{R,\mu}}{\lambda_{R,0}} - n_{0,M[N]}(\lambda_{R,\mu}) - n_\mu(\lambda_{R,\mu}) \right]^2. \quad (5.8)$$

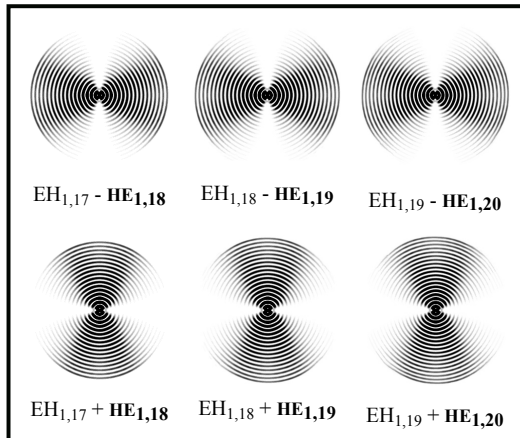
The values of M and N that minimizes the previous expression parametrize an approximation to the scaling transformation that, in a neighborhood of the initial configuration, will optimize the satisfaction of Equation 5.6 for all the considered modes.

Determining the goodness of the previous approximation requires the calculation of the associated dispersion relations and the evaluation of Equation 5.7. If χ is not small enough, the new effective refractive indices can be taken, iteratively, as a new starting point around which to minimize again Equation 5.8.

It is worth mentioning that in our simulations, the modal distribution of the HE_{1m} modes progresses in an identifiable uniform way until we reach the $HE_{1,18}$ mode where its linear polarization gradually breaks down when the strength of the field increases at large refractive index step (Ramachandran et al., 2015; Israelsen et al., 2014), as the radial and azimuthal components of the electric field must satisfy different boundary conditions (Rishøj et al., 2016).

Therefore, the electric field of the HE_{1m} modes become quasi-radially polarized, while the EH_{1m} modes become quasi-azimuthally polarized, which means, for higher mode orders the intensity distribution becomes cylindrically non-uniform which are also called bow-tie modes (Thomas et al., 2012). The three columns in Table 5.2 show the modal distribution of the

Table 5.2: The modal distribution for the bow-tie modes for the $\text{HE}_{1,18}$, $\text{HE}_{1,19}$ and $\text{HE}_{1,20}$ modes.



last three higher modes we have simulated of the type HE_{1m} , which have branched into two combinations of bow-tie modes. The merit function we use (Equations 5.7 and 5.8) deals with these bow-tie modes efficiently, while we would be able to have a very good approximation of the effective index of the required HE_{1m} mode.

However, a technical problem arises associating resonant peaks in the spectrum (see Figure 5.1) to higher-order modes, specially for the lower ones (1545 nm to 1550 nm). Figure 5.2 is an example of how the iterative process progresses when we try to identify the proper resonances (notches). Each one of the solid curves represents three iterations of the same assumption in the assignment. For example, the purple curve represents assumption number 1, in which we assume that one of the notches (like in Figure 5.1) is a resonance assigned for a specific HE_{1m} mode, which when simulated gives a specific χ value. As for the second assumption we assign the notch to another mode, for instance $\text{HE}_{1,m+1}$, and calculate the mismatch again through χ value, and so forth. The process shows an improvement in the efforts to assign the modes with their proper notches.

The last assumption we appointed is number 4 (red solid curve) where the resonances arrangement looked equitable while the χ value reached a stable low value of 3.4×10^{-3} . Moreover, if we try to assign another assumption for the resonance, we notice that χ value increases (see assumption number

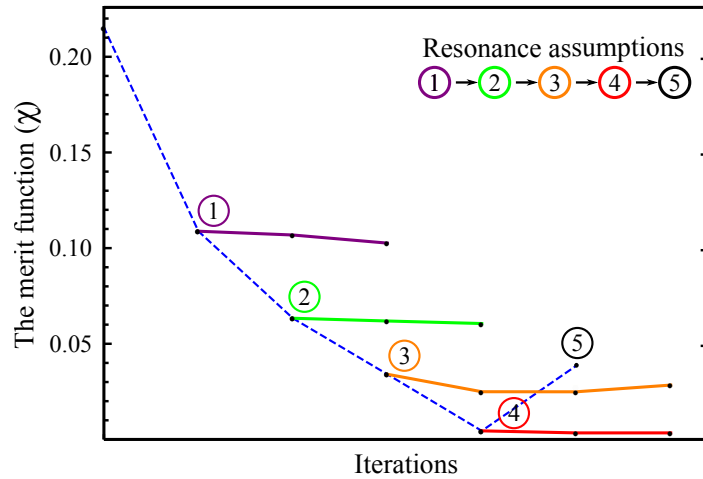


Figure 5.2: The error represented by the merit function (χ) in terms of the assigned resonances assumption, each colored solid line represent three simulation trials (black points) of the same assumption, while the dashed blue line shows the evolution χ with each resonance assumption.

5 in Figure 5.2), which means our previous resonance assigning is correct.

5.3 Effective index fitting for a BG resonances

In this last section, we show simulations of how the fiber refractive index profile changes while attempting to pin the estimated effective index points at the experimental resonance wavelengths on their corresponding simulated effective index curves. On the one hand, we will have a case of mode couplings triggered by a fiber inscribed Bragg gratings similar to the one mentioned before (Figure 5.1). On the other hand, we will show an analysis where we deal with two Bragg gratings written in the same type of fiber but with different periods.

The main goal is to proceed using the merit function defined earlier, χ , (Equation 5.8) to help us pin the estimated effective index points at the experimental resonance wavelengths on the simulated effective index curves by finding a proper fiber profile scale factors.

After identifying the first 20 HE_{1m} modes coupled in the Bragg grat-

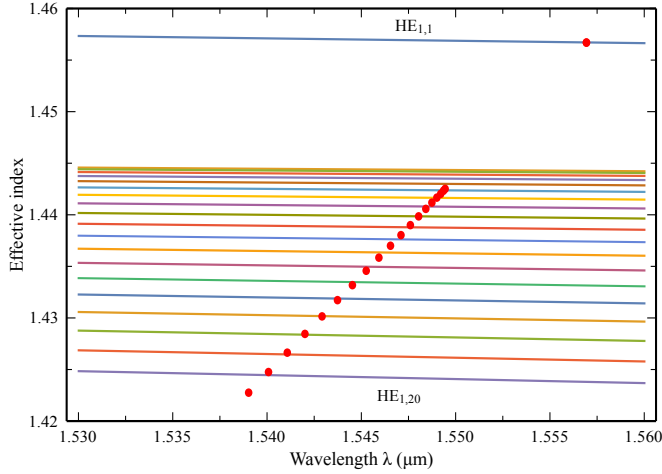


Figure 5.3: The effective index in terms of wavelength before scaling. The red points represent the estimated effective index at the experimentally calculated resonance wavelengths of the first 20 modes of the type HE_{1m} and the colored solid lines are the simulated effective index curves for the first 20 modes of the type HE_{1m} .

ing mentioned before (with $\Lambda = 533.5$ nm) and calculating the estimated effective index at each resonance wavelength, as shown in Figure 5.3, it is noticeable that, aside from the fundamental mode, the estimated effective index points at the resonance wavelengths before scaling are still not pinned properly on the simulated effective index curves.

Applying Equation 5.8, in the efforts of pinning the estimated points properly on their assigned effective index curves, will result possible values for both M and N , which means having a scaling in the geometry and refractive index difference of the fiber. In our case, the change on the core refractive index difference, Δn , would increase from 0.02883 to 0.03128 (with respect to the cladding silica refractive index at $1.55 \mu\text{m}$) and the radius is kept unscaled ($M = 1$). Therefore, an improvement in the fitting is achieved as the mismatch, represented by χ decreases from 4.8×10^{-4} to 2.5×10^{-5} . Figure 5.4 shows, after the scaling, the estimated effective index points at the experimental resonance wavelengths, which are now pinned on their corresponding effective index simulated curves.

The next simulation, and in the efforts of having a better description of

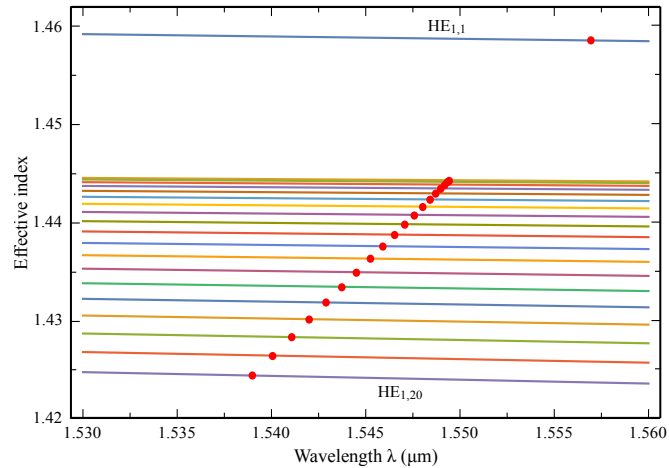


Figure 5.4: The effective index in terms of wavelength after scaling. The red points represent the estimated effective index at the experimentally calculated resonance wavelengths of the first 20 modes of the type HE_{1m} pinned on their related simulated effective index curves (colored solid lines) for the first 20 modes of the type HE_{1m} .

the fiber in a wider wavelength range, is performed on two Bragg gratings both inscribed on the SM1500 fiber used previously but each having a different grating period, which means a different working wavelength range. The first grating has a period of 521.250 nm and 1 cm length while the other has a period of 539.525 nm and 2.5 cm length. Figure 5.5 shows the transmission spectrum of both Bragg gratings each on its specific wavelength range. After the resonances have been measured experimentally by our group, we start identifying the necessary modes through the process mentioned in end of Section 5.2. Next, by initially dealing with these two gratings individually, we use Equation 5.8 to find a proper core profile scaling.

Figures 5.6 and 5.7 show, for both Bragg gratings, the estimated effective index points at the experimental resonances before (a) and after (b) being pinned on the simulated effective index curves. This fitting, as mentioned before, goes through an iterative process before reaching these results.

In Tables 5.3 and 5.4, the scaling occurred on the core radius and refractive index difference is presented, which leads to a noticeable improvement in the fitting. This improvement is also apparent through the predefined

merit function value, χ , as the mismatch between the estimated effective index points at the experimental resonances and the simulated effective index curves decreases efficiently.

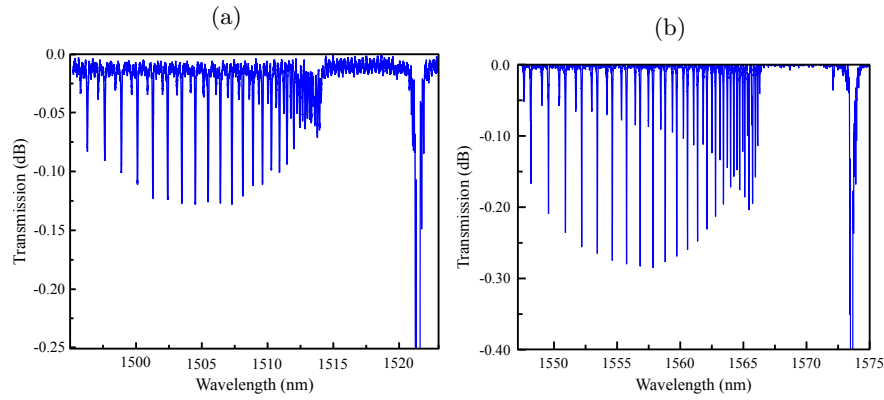


Figure 5.5: Transmission spectrum for the first (a) and the second (b) Bragg gratings.

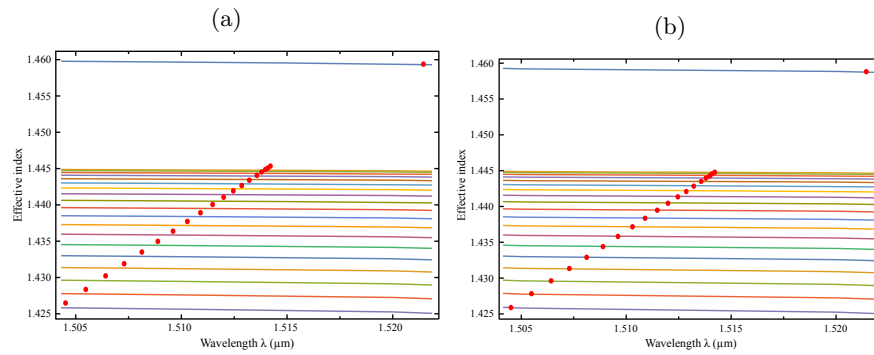


Figure 5.6: The effective index in terms of wavelength for the 1st BG. The red points are the estimated effective index at the experimental resonance wavelengths for the first 20 modes of the type HE_{1m} and the colored solid lines are the simulated effective index curves for the first 20 modes of the type HE_{1m} before scaling the core (a), and after the scaling (b) where it shows these resonances pinned properly.

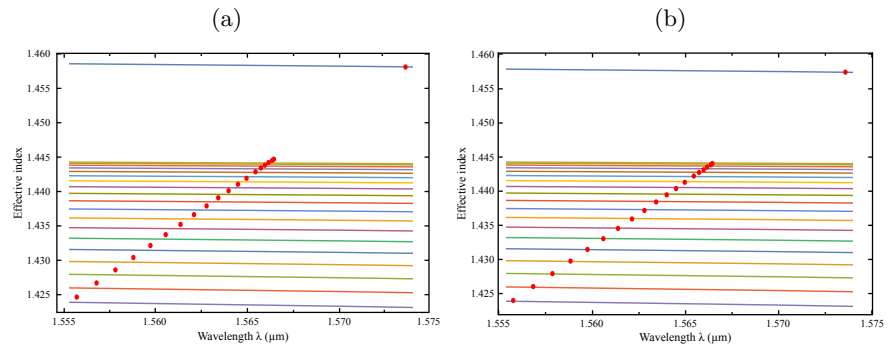


Figure 5.7: The effective index in terms of wavelength for 2^{nd} BG. The red points are the estimated effective index at the experimental resonance wavelengths for the first 20 modes of the type HE_{1m} and the colored solid lines are the simulated effective index curves for the first 20 modes of the type HE_{1m} before scaling the core (a), and after the scaling (b) where it shows these resonances pinned properly.

As noted earlier, these two Bragg gratings are inscribed on the same Fiber of the type SM1500 under very similar conditions, therefore, it would make more sense if they have the exact same fiber core parameters, radius and refractive index. For that purpose, we first assume that the new core parameters are the average of the latterly calculated two Bragg gratings, and then we iteratively apply Equation 5.8 on the new structure to improve the fitting. Simultaneously, as the change of the pinned estimated points at the resonances becomes small and sensitive, we can effectively observe the value of χ , as it is essential to obtain lower values for χ to detect an improvement in the fitting process.

Table 5.5 shows the changes occurred, through five iterations, on the core radius and refractive index difference using the scale factors M and N , until a proper averaged χ value is obtained. An averaged χ value means that with every simulated scaling we obtain a χ value for each Bragg grating, and by averaging both, we get the value of χ presented in the table. The table also shows how sensitive is the scaling effect on the system, presenting an error as small as 0.1 nm on the core radius for instance.

Figure 5.8 shows the final averaged results, as it presents, for both BGs working wavelength ranges, a very good fitting between the estimated ef-

Table 5.3: Bragg grating #1 parameters before and after the pinning.

	Before	After
Radius	1.8310 μm	1.7772 μm
Δn	0.03128	0.03125
χ	3.5×10^{-3}	5.5×10^{-5}

Table 5.4: Bragg grating #2 parameters before and after the pinning.

	Before	After
Radius	1.8310 μm	1.7589 μm
Δn	0.03128	0.03138
χ	2.2×10^{-3}	1.0×10^{-4}

Table 5.5: The iterative process applied to rescale the averaged core parameters.

Iteration	M	N	Radius (μm)	Δn	χ
1	0.99794	0.99856	1.7644	0.03125	9.7×10^{-5}
2	1.00063	1.00078	1.7657	0.03127	9.4×10^{-5}
3	1.00087	1.00107	1.7673	0.03130	8.7×10^{-5}
4	1.00042	1.00053	1.7680	0.03132	8.4×10^{-5}
5	1.00033	1.00043	1.7686	0.03133	8.3×10^{-5}

effective index points at the experimental resonances and their corresponding simulated effective index curves for all the HE_{1m} modes.

Going further in our analysis, and as it has been presented at the end of Chapter 4, we can identify the stress effect in the cladding through these mode couplings. It is expected that the stress effect would be much more sensitive than what we have experienced in the last chapter, knowing that the wavelength range we deal with in this grating analysis is smaller.

By introducing a linearly declining perturbation in the cladding refractive index similar to the one presented in Figure 4.10 with $\delta n = 0.7 \times 10^{-4}$, the resonances fitting showed an additional improvement by 8%. Figure 5.9 shows the merit function, χ , behavior when we simulated four similar fibers, each with a different value of δn . It is apparent that the δn value we assigned ranges in the lowest values of χ , which indicates a lower resonances mismatch.

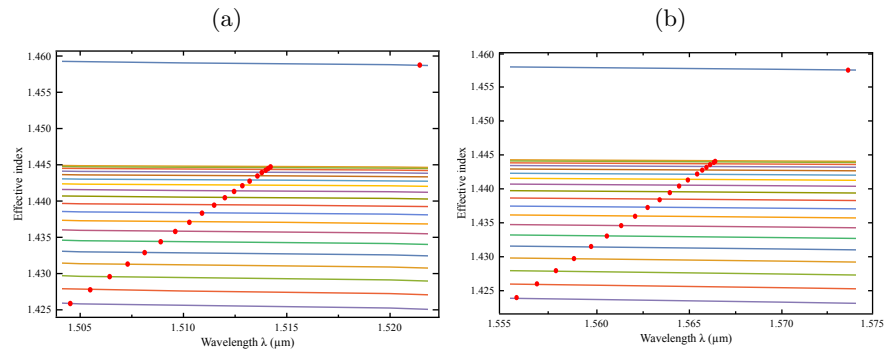


Figure 5.8: The effective index in terms of wavelength for the first Bragg gratings (a) and the second Bragg gratings (b), when Both BGs are scaled to have the exact same fiber parameters. The estimated effective index points at the experimental resonances (red points) are still properly pinned on the simulated effective index curves for the first 20 modes of the type HE_{1m} (colored solid lines).

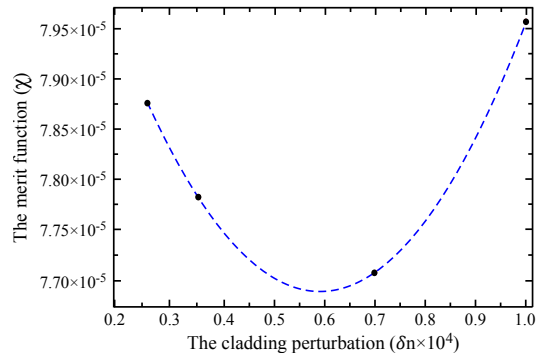


Figure 5.9: The averaged resonances mismatch, χ , in terms of the introduced perturbation value δn . The dashed blue line is an interpolation of the simulated values (black dots).

Figure 5.10 presents our last results for both BGs working wavelength ranges, where the estimated effective index points are properly pinned on the simulated effective index curves. It all leads to the conclusion that, by

using the mode couplings in these two written BGs, we were able to identify properly the core-cladding refractive index profile for the used optical fiber, and that is clearly present through a very good fitting between the estimated effective index points at the experimental resonances and the simulated effective index curves.

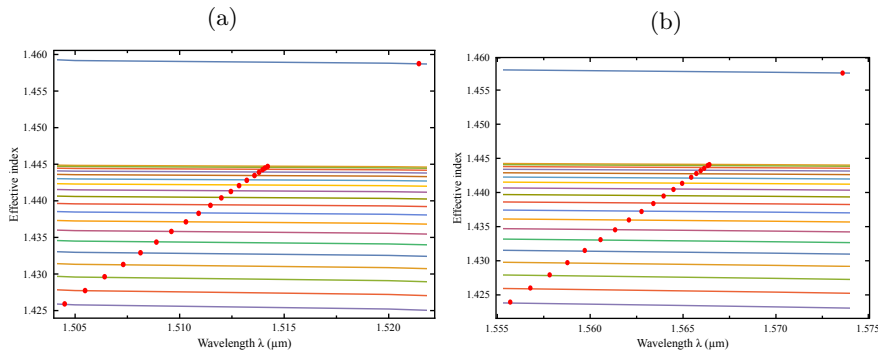


Figure 5.10: The effective index in terms of wavelength after introducing a perturbation in the cladding for the first Bragg grating (a) and the second Bragg grating (b). The estimated effective index points at the experimental resonance wavelengths (red points) are still properly pinned on the simulated effective index curves for the first 20 modes of the type HE_{1m} (colored solid lines).

Chapter 6

Conclusions

We have analyzed the core and cladding refractive index profile in standard optical fibers. The experimental data, represented by the dispersion curves and coupling resonances of the modes, have been gathered through two techniques: The first one was based on the acousto-optic interaction couplings analyzed by [Alcusa-Sáez et al. \(2016\)](#), and the second one was based on the couplings caused by an inscribed fiber Bragg gratings analyzed by [Poveda-Wong et al. \(2017\)](#).

The dispersion curves in this research hold a significant importance. Keeping in mind that, the propose of finding a better fitting for these curves is to have a better understanding of the alterations in the fiber refractive index profile. This has been addressed by investigating the scaling transformation of the optical fiber geometry and material distribution. Formerly, our group has formulated approximated analytical expressions for controlling the geometrical scaling of the fiber structure ([Pinheiro Ortega, 2008](#)). In Chapter 4 we have included the refractive index difference scaling by means of heuristic reasoning. Next, in Chapter 5, the previous approximated analytical expression has been extended to include the new degree of freedom, which, with the geometrical scaling, forms a comprehensive expression including both scale factors. This scaling approximation have paved the way for us to efficiently control the fitting of the dispersion curves and estimate the proper parameters for the optical fiber through the scale factors.

In the first case analyzed, and after realizing that a simple step index model cannot give a good match with the experiments, we took advantage of the mode couplings and the scale symmetries to, eventually, have a better

characterization for the fiber refractive index profile. The scaled fiber profile has also allowed us to fit the simulated dispersion curves with the experimental ones but only in the region below cutoff ($\lambda < \lambda_c$). Consequently, we had to introduce a perturbation in the cladding represented by a linear declining in the refractive index, which resulted after few iterations a very good fitting between the simulated and experimental curves improving by 10 times better comparing to the fiber with standard step index model, and that was analyzed in terms of both the effective index difference and the dispersion difference curves. This unconventional fiber refractive index profile have also shown that it does not only help fitting the dispersion curves for the first coupled mode but also for the higher modes of the same symmetry.

The analysis of the fibers' refractive index profile proceeded in the second part of this research work by applying our fitting approach when the mode couplings are caused by an inscribed fiber Bragg gratings on a narrower bandwidth. The Bragg grating phase matching condition has been extended and utilized into a merit function to help us identify properly the coupled modes. The same merit function would later include the scale factors so we will be able to efficiently control and estimate the required fiber scaling transformation, which ultimately pins the resonances of the coupled modes on the simulated effective index curves.

At this point of the research we needed to describe a spectrum with very large number of guided modes of a specific symmetry. Considering that our computational tool calculates all the modes in the structure, which can be in fact time consuming, we had to introduce an improvement on the computational tool using the symmetries of the vector field distribution of the modes. This improvement have helped us avoid calculating around 50% to 75% of unwanted modes, which means a significant reduction in the computational time.

In order to reduce numerical error in the profiling, the process has been applied on a single fiber Bragg grating and then on two individual Bragg gratings each with different period recorded on the same fiber. This process has proven to be efficient on both cases by decreasing the resonances average mismatch with the simulated curves by 20 to 60 times. We finally went further into identifying the stress effect in the cladding. Based on the same proposed cladding profile presented in Chapter 4, we have introduced a perturbation that, eventually, have shown an additional 8% improvement in the estimated effective index points pinning process.

The simulations in this thesis give us a clear idea on how the dispersion curves react by the change of the refractive index profile using the fiber scal-

ing properties, which ultimately will lead us to a more practical description of the fiber profile itself. The process of characterizing the fibers refractive index distribution, through the fiber scaling and cladding alteration, have also proven to be comprehensive and applicable for a wide range of commercial standard fibers.

In conclusion, we like to emphasize that due to the stress effect on the fiber during the fabrication process, the simple ideal step index model cannot describe accurately the dispersion of the fiber modes in standard fibers, specifically, when large wavelength range has to be covered. Accordingly, we have scaled the profile of the optical fiber and then investigated a modified version of the step index model, where the cladding refractive index is linearly decreasing with the radius. As a result to that modified profile, we have a perfect agreement between experimental data and theoretical simulations. This model will enable more accurate designs of long period fiber gratings, acousto-optic fiber devices, and other devices that involve the cladding modes.

Bibliography

- Abrishamian, F., Dragomir, N., & Morishita, K. (2012). Refractive index profile changes caused by arc discharge in long-period fiber gratings fabricated by a point-by-point method. *Applied Optics*, *51*, 8271–8276.
- Agrawal, G. P. (1989). *Nonlinear Fiber Optics*. Academic Press.
- Agrawal, G. P. (2002). *Fiber-optic communication systems*. Academic Press.
- Alcusa-Sáez, E. (2017). *Advanced in-fibre acousto-optics: applications*. PhD thesis, University of Valencia.
- Alcusa-Sáez, E., Díez, A., & Andrés, M. V. (2016). Accurate mode characterization of two-mode optical fibers by in-fiber acousto-optics. *Optics Express*, *24*, 4899–4905.
- Alcusa-Sáez, E. P., Díez, A., González-Herráez, M., & Andrés, M. V. (2014). Time-resolved acousto-optic interaction in singlemode optical fibers: Characterization of axial non-uniformities at the nanometer scale. *Optics Letters*, *39*, 1437–1440.
- Aspnes, D. E. (1982). Local-field effects and effective-medium theory: A microscopic perspective. *American Journal of Physics*, *50*, 704–709.
- Bates, B., Catney, M., Halliwell, D., Noble, S., & Li, Y. (1985). Transducers for ao filters: A simple technique for comparing shear wave phase of two piezoelectric transducers. *Applied Optics*, *24*, 2294–2295.
- Beltrán-Mejía, F. (2011). *Modelización de pérdidas por radiación en dispositivos de fibra microestructurada. aplicaciones*. PhD thesis, University of Valencia.

- Berwick, M., Pannell, C. N., Russell, P. S. J., & Jackson, D. A. (1991). Demonstration of birefringent optical fibre frequency shifter employing torsional acoustic waves. *Electronics Letters*, *27*, 713–715.
- Birks, T. A., Russell, P. S. J., & Culverhouse, D. O. (1996). The acousto-optic effect in single-mode fiber tapers and couplers. *Journal of Lightwave Technology*, *14*, 2519–2529.
- Blake, J. N., Kim, B. Y., Engan, H. E., & Shaw, H. J. (1987). Analysis of intermodal coupling in a two-mode fiber with periodic microbends. *Optics Letters*, *12*, 281–283.
- Blake, J. N., Kim, B. Y., & Shaw, H. J. (1986). Fiber-optic modal coupler using periodic microbending. *Optics Letters*, *11*, 177–179.
- Block, U. L., Dangui, V., Digonnet, M. J. F., & Fejer, M. M. (2006). Origin of apparent resonance mode splitting in bent long-period fiber gratings. *Journal of Lightwave Technology*, *24*, 1027–1034.
- Chang, I. C. (1976). Acoustooptic devices and applications. *IEEE Transactions on Sonics and Ultrasonics*, *23*, 2–21.
- Cuadrado-Laborde, C., Díez, A., Cruz, J. L., & V., A. M. (2010). Experimental study of an all-fiber laser actively mode-locked by standing-wave acousto-optic modulation. *Applied Physics B: Lasers and Optics*, *99*, 95–99.
- Davis, C. M. (1985). Fiber optic sensors: An overview. *Optical Engineering*, *24*, 242347–242352.
- Díez, A., Birks, T. A., Reeves, W. H., Mangan, B. J., & Russell, P. S. J. (2000). Excitation of cladding modes in photonic crystal fibers by flexural acoustic waves. *Optics Letters*, *25*, 1499–1501.
- Engan, H. E. (1996). Analysis of polarization-mode coupling by acoustic torsional waves in optical fibers. *Journal of the Optical Society of America A*, *13*, 112–118.
- Erdogan, T. (1997a). Cladding-mode resonances in short- and long-period fiber grating filters. *Journal of the Optical Society of America A*, *14*, 1760–1773.

- Erdogan, T. (1997b). Fiber grating spectra. *Journal of Lightwave Technology*, *15*, 1277–1294.
- Erdogan, T. (1999). Cladding-mode resonances in short- and long-period fiber grating filters. *Journal of the Optical Society of America A*, *14*, 1760–1773.
- Erdogan, T. & Sipe, J. E. (1996). Tilted fiber phase gratings. *Journal of the Optical Society of America A*, *13*, 296–313.
- Ferrando, A., Silvestre, E., Andrés, P., Miret, J. J., & Andrés, M. V. (2001). Designing the properties of dispersion-flattened photonic crystal fibers. *Optics Express*, *9*, 687–697.
- Fleming, J. W. (1984). Dispersion in GeO₂-SiO₂ glasses. *Applied Optics*, *23*, 4486–4493.
- Frigo, M. & Johnson, S. (1998). FFTW: an adaptive software architecture for the FFT. In *Proceedings of the 1998 IEEE International Conference on Acoustics, Speech and Signal Processing*.
- Gambling, W. A., Payne, D. N., & Matsumura, H. (1977). Effect of dip in the refractive index on the cut-off frequency of a single-mode fibre. *Electronics Letters*, *13*, 174–175.
- Gantmacher, F. R. (1966). *Théorie des Matrices*. Dunod.
- Gloge, D. (1971). Weakly guiding fibers. *Applied Optics*, *10*, 2252–2258.
- Gowar, J. (1993). *Optical Communication Systems*. Prentice Hall.
- Guo, T., Ivanov, A., Chen, C., & Albert, J. (2008). Temperature-independent tilted fiber grating vibration sensor based on cladding-core recoupling. *Optics Letters*, *33*, 1004–1006.
- Guo, T., Shao, L., Tam, H. Y., Krug, P. A., & Albert, J. (2009). Tilted fiber grating accelerometer incorporating an abrupt biconical taper for cladding to core recoupling. *Optics Express*, *17*, 20651–20660.
- Haakestad, M. & Engan, H. (2006). Acoustooptic properties of a weakly multimode solid core photonic crystal fiber. *Journal of Lightwave Technology*, *24*, 838–845.
- Haus, H. A. (1984). *Waves and Fields in Optoelectronics*. Prentice Hall.

- Hill, K. O., Fujii, Y., Johnson, D. C., & Kawasaki, B. S. (1978). Photosensitivity in optical fiber waveguides: Application to reflection filter fabrication. *Applied Physics Letters*, *32*, 647–649.
- Hill, K. O., Malo, B., Vineberg, K. A., Bilodeau, F., Johnson, D. C., & Skinner, I. (1990). Efficient mode conversion in telecommunication fibre using externally written gratings. *Electronics Letters*, *26*, 1270–1272.
- Huang, W.-P. (1994). Coupled-mode theory for optical waveguides: An overview. *Journal of the Optical Society of America A*, *11*, 963–983.
- Israelsen, S. M., Rishøj, L. S., & Rottwitt, K. (2014). Break up of the azimuthal symmetry of higher order fiber modes. *Optics Express*, *22*, 11861–11868.
- Jenkins, F. A. & White, H. E. (1957). *Fundamentals of optics*. McGraw-Hill.
- Jing, N., Zheng, J., Zhao, X., & Teng, C. (2014). Investigation of a macrobending micro-plastic optical fiber for refractive index sensing. *Applied Optics*, *53*, 8145–8150.
- Joannopoulos, J. D., Johnson, S. G., Meade, R. D., & Winn, J. N. (2008). *Photonic crystals: molding the flow of light*. Princeton University Press.
- Johnson, S. & Joannopoulos, J. (2001). Block-iterative frequency-domain methods for maxwell's equations in a planewave basis. *Optics Express*, *8*, 173–190.
- Jones, A. L. (1965). Coupling of optical fibers and scattering in fibers. *Journal of the Optical Society of America*, *55*, 261–271.
- Jung, I. W., Park, B., Provine, J., Howe, R. T., & Solgaard, O. (2011). Highly sensitive monolithic silicon photonic crystal fiber tip sensor for simultaneous measurement of refractive index and temperature. *Journal of Lightwave Technology*, *29*, 1367–1374.
- Kapany, N. S. (1967). *Fiber Optics: Principles and Applications*. Academic Press.
- Kashyap, R. (1999). *Fiber Bragg Gratings*. Academic Press.
- Keiser, G. (2000). *Optical Fiber Communications*. McGraw-Hill.

- Kim, H. S., Yun, S. H., Kwang, I. K., & Kim, B. Y. (1997). All-fiber acousto-optic tunable notch filter with electronically controllable spectral profile. *Optics Letters*, *22*, 1476–1478.
- Kitayama, K. & Ikeda, M. (1978). Mode coupling coefficient measurements in optical fibers. *Applied Optics*, *17*, 3979–3983.
- Kogelnik, H. (1975). *Theory of dielectric waveguides*. Springer.
- Lee, D. L. (1986). *Electromagnetic Principle of Integrated Optics*. Wiley.
- Lee, K. & Erdogan, T. (2001). Fiber mode conversion with tilted gratings in an optical fiber. *Journal of the Optical Society of America A*, *18*, 1176–1185.
- Lee, K. J., Hwang, I. K., Park, H. C., & Kim, B. Y. (2009). Axial strain dependence of all-fibre acousto-optic tunable filters. *Optics Express*, *17*, 2348–2357.
- Lee, K. J., Park, H. C., & Kim, B. Y. (2007). Highly efficient all-fiber tunable polarization filter using torsional acoustic wave. *Optics Express*, *15*, 12362–12367.
- Lee, K. S. & Erdogan, T. (2000). Fiber mode coupling in transmissive and reflective tilted fiber gratings. *Applied Optics*, *39*, 1394–1404.
- LFO. Laboratory of fiber optics. <http://www.uv.es/lfo>.
- Light, P. S., Roberts, P. J., Mirault, P., & Benabid, F. (2008). Observation of anti-crossing events via mode-pattern rotation in HC-PCF. In *Conference on Lasers and Electro-Optics and 2008 Conference on Quantum Electronics and Laser Science*.
- Lillywhite, P. G. (1978). Coupling between locust photoreceptors revealed by a study of quantum bumps. *Journal of comparative physiology*, *125*, 13–27.
- Lin, C. Y., Wang, L. A., & Chern, G. W. (2001). Corrugated long-period fiber gratings as strain, torsion, and bending sensors. *Journal of Light-wave Technology*, *19*, 1159–1168.
- Liu, W. F., Liu, I. M., Chung, L. W., Huang, D. W., & Yang, C. C. (2000). Acoustic-induced switching of the reflection wavelength in a fiber bragg grating. *Optics Letters*, *25*, 1319–1321.

- Louisell, W. H. (1960). *Coupled-Mode and Parametric Electronics*. Wiley.
- Luo, Z., Ye, C., Cai, Z., Dai, X., Kang, Y., & Xu, H. (2007). Numerical analysis and optimization of optical spectral characteristics of fiber bragg gratings modulated by a transverse acoustic wave. *Applied Optics*, *46*, 6959–6965.
- Marcuse, D. (1973). Coupled mode theory of round optical fibers. *The Bell System Technical Journal*, *52*, 817–842.
- Marcuse, D. (1982). Influence of curvature on the losses of doubly clad fibers. *Applied Optics*, *21*, 4208–4213.
- Marcuse, D. (1991). *Theory of Dielectric Optical Waveguides*. Elsevier.
- Martinez, A., Lai, Y., Dubov, M., & Khrushchev, I. (2005). Vector bending sensors based on fibre bragg gratings inscribed by infrared femtosecond laser. *Electronics Letters*, *41*, 472–474.
- McCall, M. (2000). On the application of coupled mode theory for modeling fiber bragg gratings. *Journal of Lightwave Technology*, *18*, 236–242.
- Miller, S. E. (1954). Coupled wave theory and waveguide applications. *The Bell System Technical Journal*, *33*, 661–719.
- Mollenauer, L. F., Mamyshev, P. V., & Neubelt, M. J. (1996). Method for facile and accurate measurement of optical fiber dispersion maps. *Optics Letters*, *21*, 1724–1726.
- Morse, P. M. & Feshbach, H. (1953). *Methods of Theoretical Physics*. McGraw-Hill.
- Nakajima, K., Ohashi, M., & Tateda, M. (1997). Chromatic dispersion distribution measurement along a single-mode optical fiber. *Journal of Lightwave Technology*, *15*, 1095–1101.
- Olshansky, R. & Keck, D. B. (1976). Pulse broadening in graded-index optical fibers. *Applied Optics*, *15*, 483–491.
- Östling, D. & Engan, H. E. (1995). Narrow-band acousto-optic tunable filtering in a two-mode fiber. *Optics Letters*, *20*, 1247–1249.

- Paiva, C. R. & Barbosa, A. M. (1992). A linear-operator formalism for the analysis of inhomogeneous biisotropic planar waveguides. *Journal of Lightwave Technology*, *10*, 728–734.
- Pang, F., Xiang, W., Guo, H., Chen, N., Zeng, X., Chen, Z., & Wang, T. (2008). Special optical fiber for temperature sensing based on cladding-mode resonance. *Optics Express*, *16*, 12967–12972.
- Paurisse, M., Lévêque, L., Hanna, M., Druon, F., & Georges, P. (2012). Complete measurement of fiber modal content by wavefront analysis. *Optics Express*, *20*, 4074–4084.
- Pei, L., Liu, C., Li, J., Zheng, J., Yu, S., & Wu, L. (2014). Highly sensitive axial strain fiber laser sensor based on all-fiber acousto-optic tunable filter. *IEEE Photonics Technology Letters*, *26*, 2430–2433.
- Pierce, J. R. (1954). Coupling of modes of propagation. *Journal of Applied Physics*, *25*, 179–183.
- Pinheiro Ortega, T. (2008). *Análisis y diseño avanzados en fibras de cristal fotónica*. PhD thesis, University of Valencia.
- Poveda-Wong, L., Cruz, J. L., Delgado-Pinar, M., Roselló-Mechó, X., Díez, A., & Andrés, M. V. (2017). Fabrication of long period fiber gratings of subnanometric bandwidth. *Optics Letters*, *42*, 1265–1268.
- Presby, H. M. (1977). Detection of geometric perturbations in optical fibers. *Applied Optics*, *16*, 695–700.
- Primak, W. & Post, D. (1959). Photoelastic constants of vitreous silica and its elastic coefficient of refractive index. *Journal of Applied Physics*, *30*, 779–788.
- Rahman, B. M. A., Mishra, J. K., & Pan, C. (2018). Design and optimization of photonic devices and optical fibers for space-division multiplexing. *Proceedings of SPIE*, *10560*, 7–18.
- Ramachandran, S., Gregg, P., Kristensen, P., & Golowich, S. E. (2015). On the scalability of ring fiber designs for oam multiplexing. *Optics Express*, *23*, 3721–3730.

- Ramírez-Meléndez, G., Bello-Jiménez, M., Cuadrado-Laborde, C., Díez, A., Cruz, J., Rodríguez-Cobos, A., Balderas-Navarro, R., & Andrés, M. V. (2016). Acousto-optic interaction in biconical tapered fibers: Shaping of the stopbands. *Optical Engineering*, *55*, 55–63.
- Rishøj, L., Jones, M., Demas, J., Gregg, P., Prabhakar, G., Yan, L., Hawkins, T., Ballato, J., & Ramachandran, S. (2016). Polymer-clad silica fibers for tailoring modal area and dispersion. *Optics Express*, *41*, 3587–3590.
- Saad, Y. (1992). *Numerical Methods for Large Eigenvalue Problems*. Manchester University.
- Sáez-Rodríguez, D., Cruz, J. L., Díez, A., & Andrés, M. V. (2011). Coupling between counterpropagating cladding modes in fiber bragg gratings. *Optics Letters*, *36*, 1518–1520.
- Saleh, B. E. A. & Teich, M. C. (2001). *Fundamentals of Photonics*. Wiley.
- Savovic, S. & Djordjevich, A. (2007). Method for calculating the coupling coefficient in step-index optical fibers. *Applied Optics*, *46*, 1477–1481.
- Schmidt, F. & Petermann, K. (2017). Investigation of LP- and vector-modes for the analysis of space-division multiplexed systems in the nonlinear regime. *Journal of Lightwave Technology*, *35*, 4859–4864.
- Serway, R. A., Moses, C. J., & Moyer, C. A. (1957). *Modern Physics*. Saunders College Publishing.
- Shen, Y. R. (1984). *Principles of Nonlinear Optics*. Wiley.
- Siegman, A. E. (1986). *Lasers*. University Science Books.
- Silvestre, E., Andres, M. V., & Andres, P. (1998). Biorthonormal-basis method for the vector description of optical-fiber modes. *Journal of Lightwave Technology*, *16*, 923–928.
- Silvestre, E., Pinheiro-Ortega, T., Andrés, P., Miret, J. J., & Ángela Coves (2006). Differential toolbox to shape dispersion behavior in photonic crystal fibers. *Optics Letters*, *31*, 1190–1192.
- Silvestre, E., Pinheiro-Ortega, T., Andrés, P., Miret, J. J., & Ortigosa-Blanch, A. (2005). Analytical evaluation of chromatic dispersion in photonic crystal fibers. *Optics Letters*, *30*, 453–455.

- Skaar, J. & Waagaard, O. H. (2003). Design and characterization of finite length fiber gratings. *IEEE Journal of Quantum Electronics*, *39*, 1238–1245.
- Smith, A. M. (1980). Birefringence induced by bends and twists in single-mode optical fiber. *Applied Optics*, *19*, 2606–2611.
- Snyder, A. W. (1969). Asymptotic expressions for eigenfunctions and eigenvalues of a dielectric or optical waveguide. *IEEE Transactions on Microwave Theory and Techniques*, *17*, 1130–1138.
- Snyder, A. W. (1972). Coupled-mode theory for optical fibers. *Journal of the Optical Society of America*, *62*, 1267–1277.
- Snyder, A. W. & Love, D. J. (1983). *Optical Waveguide Theory*. Chapman and Hall.
- Tamir, T. (1988). *Guided-Wave Optoelectronics*. Springer.
- Tashtush, A., Silvestre, E., Díez, A., Cruz, J. L., & Andrés, M. V. (2019). Analysis of effective core and cladding refractive index profile in standard single mode fibers: matching the experimental dispersion curves. Unpublished.
- Thomas, J., Jovanovic, N., Becker, R. G., Marshall, G. D., Withford, M. J., Tünnermann, A., Nolte, S., , & Steel, M. J. (2011). Cladding mode coupling in highly localized fiber bragg gratings: modal properties and transmission spectra. *Optics Express*, *19*, 325–341.
- Thomas, J. U., Jovanovic, N., Krämer, R. G., Marshall, G. D., Withford, M. J., Tünnermann, A., Nolte, S., & Steel, M. J. (2012). Cladding mode coupling in highly localized fiber bragg gratings II: complete vectorial analysis. *Optics Express*, *20*, 21434–21449.
- Vegsarkar, A. M., Lemaire, P. J., Judkins, J. B., Bhatia, V., Erdogan, T., & Sipe, J. E. (1996). Long-period fiber gratings as band-rejection filters. *Journal of Lightwave Technology*, *14*, 58–65.
- Vengsarkar, A. M., Lemaire, P. J., Judkins, J. B., Bhatia, V., Erdogan, T., & Sipe, J. E. (1996). Long-period fiber gratings as band-rejection filters. *Journal of Lightwave Technology*, *14*, 58–65.

- Violakis, G., Aggarwal, N., & Limberger, H. G. (2012). Stress changes in H₂-loaded SMF optical fibers induced by cw-Ar⁺ 244 nm irradiation. *Optical Materials Express*, *2*, 1490–1495.
- Vita, P. D. & Rossi, U. (1979). Backscattering measurements in optical fibres: separation of power decay from imperfection contribution. *Electronics Letters*, *15*, 467–469.
- Wang, Z. L., Ogura, H., & Takahashi, N. (1995). Radiation and coupling of guided modes in an optical fiber with a slightly rough boundary: stochastic functional approach. *Journal of the Optical Society of America A*, *12*, 1489–1500.
- Yariv, A. (1973). Coupled-mode theory for guided-wave optics. *IEEE Journal of Quantum Electronics*, *9*, 919–933.
- Yin, G., Lou, S., Li, Q., & Zou, H. (2013). Theory analysis of mode coupling in tilted long period fiber grating based on the full vector complex coupled mode theory. *Optics and Laser Technology*, *48*, 60–66.
- Zangaro, R. A., Silveira, L., & da Silva, R. B. (1995). Optical fiber sensor for the measurement of stress in concrete structures. *Measurement*, *16*, 103–105.
- Zemon, S. A. & Dakks, M. L. (1978). Acoustooptic modulator for optical fiber waveguides. *U.S. Patent*, 4068191.
- Zhang, X., Xie, L., Zhang, Y., & Peng, W. (2015). Optimization of long-period grating-based refractive index sensor by bent-fiber interference. *Applied Optics*, *54*, 9152–9156.
- Zhao, Y., Xia, F., & Li, J. (2016). Sensitivity-enhanced photonic crystal fiber refractive index sensor with two waist-broadened tapers. *Journal of Lightwave Technology*, *34*, 1373–1379.
- Zou, X., Li, M., Pan, W., Yan, L., Azaña, J., & Yao, J. (2013). All-fiber optical filter with an ultranarrow and rectangular spectral response. *Optics Letters*, *38*, 3096–3098.